LAWRENCE
LIVERMORE
NATIONAL
LABORATORY

LLNL-JRNL-806201

The Role of Redox on Bridgmanite Crystal Chemistry and Calcium Speciation in the Lower Mantle

N. Creasy, J. Girard, K. K. M. Lee

March 3, 2020

Journal of Geophysical Research, Solid Earth

Disclaimer

The Role of Redox on Bridgmanite Crystal Chemistry and Calcium Speciation in the Lower Mantle

Neala Creasy[1,2*], Jennifer Girard[1], James O. Eckert, Jr.,[1] and Kanani K. M. Lee[1,3]

[1]Department of Earth and Planetary Sciences, Yale University, New Haven, CT, USA, [2]Department of Geophysics, Colorado School of Mines, Golden, CO, USA, [3]Lawrence Livermore National Laboratory, Livermore, CA, USA

Corresponding author: Neala Creasy (nmcreasy@mines.edu)

Key Points:

- Al-rich pyroxenite mineralogy, density, and seismic velocity are tied to ferric iron content at lower mantle conditions
- Ferric iron and aluminum content may affect the formation of calcium-bearing bridgmanite

Abstract: Words – 235, Max is 250.

The amount of ferric iron Fe^{3+} in the lower mantle is largely unknown and may be influenced by the disproportionation reaction of ferrous iron Fe^{2+} into metallic Fe and Fe^{3+} triggered by the formation of bridgmanite. Recent work has shown that Fe^{3+} has a strong effect on the density and seismic wave speeds of bridgmanite and the incorporation of impurities such as aluminum. In order to further investigate the effects of ferric iron on mineral behavior at lower mantle conditions, we conducted laser-heated diamond-anvil cell (LHDAC) experiments on two sets of samples nearly identical in composition (an aluminum-rich pyroxenite glass) except for the Fe^{3+} content; with one sample with more Fe^{3+} ("oxidized": $Fe^{3+}/\Sigma Fe \sim 55\%$) and the other with less Fe^{3+} ("reduced": $Fe^{3+}/\Sigma Fe \sim 11\%$). We heated the samples to lower mantle conditions, and the resulting assemblages were drastically different between the two sets of samples. For the reduced composition, we observed a multiphase assemblage dominated by bridgmanite and calcium perovskite. In contrast, the oxidized material yielded a single phase of Ca-bearing bridgmanite. These Al-rich pyroxenite samples show a difference in density and seismic velocities for these two redox states, where the reduced assemblage is denser than the oxidized assemblage by ~1.5 % at the bottom of the lower mantle and slower (bulk sound speed) by ~2%. Thus, heterogeneities of Fe^{3+} content may lead to density and seismic wave speed heterogeneities in the Earth's lower mantle.

Plain Language Summary: Words – 197, Max is 200

Iron primarily exists in three oxidation states within the mantle: metallic iron (Fe^0), ferrous iron Fe^{2+} (more reduced form) and ferric iron Fe^{3+} (more oxidized form), however, the amount of Fe^{3+} in the lower mantle is largely unknown. Recent work has shown that Fe^{3+} has a strong effect on rock density and speed at which seismic waves travel through lower mantle minerals. In order to further investigate these effects, we conducted experiments on samples nearly identical in composition except for the Fe^{3+} content. We compressed the samples between two diamonds and heated the sample to the conditions of Earth's lower mantle. For the reduced sample (low Fe^{3+} content), we observed a complex assemblage of minerals, primarily composed of bridgmanite (the most abundant mineral in the Earth) and calcium silicate perovskite (a common secondary phase in the lower mantle). In contrast, the oxidized sample (high Fe^{3+} content) yielded a single phase of these two minerals combined together as one mineral – a Ca-bearing bridgmanite. The resulting oxidized sample is lighter and seismic waves travel faster through it than the reduced sample. Thus, changes in Fe^{3+} content may lead to density and seismic wave speed variations in Earth's lower mantle.

1 Introduction

In all compositional models of the lower mantle, the most abundant mineral is expected to be a magnesium-rich silicate perovskite (nominally, $(Mg,Fe)SiO_3$) known as bridgmanite (Tschauner et al., 2014). As such, the crystal chemistry of bridgmanite largely determines the physical properties of the lower mantle such as density, seismic velocities, and rheology. Recently, the ferric iron Fe^{3+} content in bridgmanite has been found to affect bridgmanite and secondary minerals (Gu et al., 2016; Shim et al., 2017; Kurnosov et al., 2017). However, the relative amount of ferric iron Fe^{3+} (i.e., a measure of oxidation state) present in the lower mantle is unknown, with estimates that vary between 13 and 60% (Kurnosov et al., 2017; Frost and McCammon, 2008). Diamond inclusions suggest that the oxygen fugacity may vary by up to ten log units in the lower mantle (Kaminsky et al., 2015). It is well known that Fe^{3+}, in addition to aluminum Al^{3+}, is soluble in bridgmanite; thus, Fe^{3+} must play a role in the chemistry and dynamics of the lower mantle (e.g., Andrault et al., 2018). While there is abundant information on bridgmanite and the incorporation of Fe^{3+} into its structure (e.g., McCammon, 1997; Catalli et al., 2011; Frost and McCammon, 2008), there is relatively little understanding on the effects of Fe^{3+} on the overall mineralogy and properties of the resulting assemblage (Gu et al., 2016).

While the mantle is heterogeneous (e.g., van Keken et al., 2002), it is often assumed to be pyrolitic in composition (Irifune & Tsuchiya, 2015). The lower mantle, if pyrolite-like in composition, would result in bridgmanite $(Mg,Fe)SiO_3$ (~76 mol%), ferropericlase (Mg,Fe)O (~17%), and calcium perovskite $CaSiO_3$ (~7%) phases (e.g., Lee et al., 2004). Multiple studies on the bridgmanite structure have shown a high solubility of Fe^{3+}, much more than bridgmanite's low-pressure predecessors: olivine, wadsleyite, and ringwoodite (as summarized in Frost and McCammon, 2008). However, there are few constraints on actual Fe^{3+} content in the Earth's lower

mantle (Frost and McCammon, 2008; Shim et al., 2017). Therefore, regions with varying Fe^{3+} content may show other characteristics that could be imaged seismically, such as a difference in density and seismic velocities (Gu et al., 2016).

Recent work by Kurnosov et al., (2017) shows that a decrease of Fe^{3+} content (66% to 33%) in the bridgmanite structure in a pyrolite model agrees with the Preliminary Reference Earth Model (PREM) (Dziewonski & Anderson, 1981) from a depth of 800 to 1,200 km, whereas a pyrolite model with only Fe^{2+} does not agree as well with PREM. In addition, we expect a mineralogical effect to be observed with changing Fe^{3+} based on recent results (Gu et al., 2016). In that study, under conditions with low Fe^{3+} abundance ($Fe^{3+}/\Sigma Fe$ ~30%), Al_2O_3 exsolved as a separate phase, whereas with greater amounts of Fe^{3+} ($Fe^{3+}/\Sigma Fe$ ~35%), all of the alumina was incorporated into the bridgmanite phase (Gu et al., 2016). Due to the coupled substitution of Fe^{3+} and Al^{3+} into the bridgmanite structure, more Fe^{3+} in the material leads to an increase in Al^{3+} solubility by bridgmanite (Frost et al., 2004). However, it is unknown how Fe^{3+} content affects other mantle assemblages, such as basalt, peridotite, pyroxenite, and pyrolite (Ko et al., 2017), when many of the resulting lower mantle assemblages assume iron exists only in the Fe^{2+} state.

Ferric iron may have other impacts as well on bridgmanite crystal chemistry. The large miscibility gap between $MgSiO_3$-bridgmanite and $CaSiO_3$-perovskite has been well documented through experiments (Armstrong et al., 2012; Irifune et al., 1989; Tamai and Yagi, 1989) and *ab initio* computations (Jung and Schmidt, 2011), yielding at most ~1 mol% Ca incorporation into $MgSiO_3$. However, the combined effect of Al and Fe^{3+} effects on the solubility of bridgmanite and calcium perovskite were beyond the scope of those studies. While many studies have used samples that included Al and Fe^{3+} to investigate lower mantle mineralogy for MORB and pyrolite (e.g., Dorfman et al., 2013; Gu et al., 2016; Lee et al., 2004; Nishiyama and Yagi, 2003; Ono et al.,

2001; Ricolleau et al., 2010), nearly every study that has included calcium has found calcium perovskite to form as an independent phase or if calcium is present in small amounts can take up ~1 mol% within the bridgmanite unit cell and ~3 mol% of Mg into the calcium perovskite unit cell. One exception is recent work by Ko et al. (2017), where they attempt to constrain pyrolite mineralogy under different redox conditions and is strongly dependent on Fe and Al content of bridgmanite. Miyajima et al. (1999) placed natural garnets into a multi-anvil press and found one garnet series produced a Mg-perovskite with 6-7 mol% Ca with a calculated $Fe^{3+}/\Sigma Fe$ greater than 80%. Fujino et al. (2004) observed a calcium perovskite with 9 Mg and 8 mol% Fe when compressing a diopside to mid-mantle pressures (i.e., 78 GPa). Therefore, there appears to be an unknown relationship between the combined effects of Al, Fe^{2+}, Fe^{3+}, Ca, and the miscibility gap between bridgmanite and calcium perovskite when Fe^{3+} is abundant, where under rare circumstances Mg- and Ca-perovskites appear to be soluble.

In this study, we investigated the effect of Fe^{3+} on the density and mineralogy of a plausible mantle rock composition, an Al-rich pyroxenite. Pyroxenites encompass a wide class of rocks that consists of pyroxenes and garnets that are possible parent bodies that melt at shallow depths to form ocean island basalts (e.g., MIX1G: Hirschmann et al., 2003; Kogiso & Hirschmann, 2006) (see Table 1, Figure S3). Additionally, there is evidence that hot spots (e.g., Hawaii) have their origins at much greater depths (e.g., Jackson et al., 2018). Pyroxenites are typically higher in Al and Ca and lower in Mg content compared to pyrolite but vary widely in composition and ferric iron content (Hirschmann et al., 2003). Incidentally, pyrolite falls within the high end of MgO content pyroxenites (Figure S3). Therefore, pyroxenite is a plausible lower mantle assemblage that is present within the mantle, at least at some concentration (Mallik et al., 2020). It is important to test a range of plausible chemistries in the mantle since the mantle is not

119 homogenous as is evident in seismic tomography studies (e.g., Deschamps et al., 2015 & Kaminski
120 and Javoy, 2015). The mantle is chemically heterogeneous and an average pyrolitic model does
121 not convey its complexity. Additionally, oxidation state appears to play a large role in mineralogy
122 and the crystal structure of bridgmanite (e.g., Gu et al., 2016 Catalli et al., 2010; Kurnosov et al.,
123 2017). As the disproportionation of iron in the lower mantle may occur during the transition of
124 olivine into bridgmanite and ferropericlase (Frost et al., 2004), the ferric iron content within
125 bridgmanite appears to change with depth (Shim et al., 2017). Additionally, subduction processes
126 may also affect the local oxidation state of the mantle. This study attempts to explore mantle
127 complexity by investigating how ferric iron affects mineralogy beyond the canonical pyrolitic
128 mantle composition.

129 Following Gu et al. (2016), we considered a material that has a larger contrast in Fe^{3+}
130 content ($Fe^{3+}/\Sigma Fe \sim 55\%$ vs. ~11%) and with more Al^{3+} and Fe in order to amplify any potential
131 differences in density and mineralogy observed previously (Gu et al., 2016) (Table 1). While the
132 compositions we study are not likely to comprise the majority of the mantle (i.e., quite different
133 from the canonical pyrolite model), pyroxenites may yield ocean island basalts when partially
134 melted (Hirschmann et al., 2003) which are expected to come from deep within the mantle. Based
135 on our measurements and Monte Carlo modeling , we used Burnman (Cottaar et al., 2014), a
136 Python toolkit, to calculate the density and bulk sound speed profiles of the resulting mineral
137 assemblages.

138

139 **2 Materials and Methods**

140 We use the LHDAC to simulate the high pressures and temperatures of the lower mantle.
141 We conducted multiple experiments on two separate sets of glass samples which differed in Fe^{3+}

content with one reducing (MIX_RED, $Fe^{+3}/\sum Fe \sim 11\%$) and one more oxidizing (MIX_OX, $Fe^{+3}/\sum Fe \sim 55\%$) (Table 1) as determined by Mössbauer spectroscopy (Figure S1, Supporting Information: Section I). Both glass samples (see Figure S2) were synthesized by laser levitation while in a controlled gas environment to vary oxygen fugacity and thus ferric iron content (Gu et al., 2016). As there was some volatile loss during the laser levitation process, the samples are not identical to MIX1G reported in Hirschmann et al. (2003); however, the samples' bulk compositions are within the class of natural pyroxenites (Table 1 and Figure S3). As a result of volatile loss, our samples are relatively enriched in Al_2O_3, compared to other pyroxenites, thus we refer to our samples as Al-rich pyroxenites.

Each glass bead sample was cut in half, polished, and the composition was determined by electron probe microanalysis (EPMA) (Tables 1, S1, S2, see Supporting Information: Section II) prior to being powdered and sample prepared with stepped anvils (Du et al., 2015). The stepped samples are then transferred to a diamond-anvil cell equipped with opposing flat culet anvils, which is then loaded with neon to provide thermal insulation and *in situ* pressure calibration (Zhuravlev et al., 2013). Stepped anvil cells allow for simple loading of gases with even thermal insulation layers and give the ability to recover the sample more easily for EPMA analyses as the samples are pressed into the gasket. Prior to the initial laser heating of the glass samples for assemblage synthesis, the presence of Ne in each sample is confirmed by XRD. In the collected high-pressure XRD patterns after laser heating (Figures 1, S5-S6), neon is not always easy to identify due to overlap with other synthesized phases present; therefore, we also use Raman spectroscopy of the diamond anvils to determine pressure before and after heating (Akahama & Kawamura, 2006). We report both measurements of pressures but use the pressures determined by diamond Raman with uncertainties defined by the difference between the pressures determined by

each method (Tables S6 and S7). At the highest pressures reached in our study, the pressures differ by up to 6 GPa, with pressures determined by Raman greater than those determined by neon.

We collected *in situ* x-ray diffraction (XRD) (Figure 1) to reveal the mineralogy and compressibility of the samples at the HPCAT-IDB beamline (λ=0.406626 Å) at the Advanced Photon Source (APS) at Argonne National Laboratory (Meng et al., 2015) (Supporting Information, Section VII). Two samples each of the MIX_RED and MIX_OX compositions were synthesized between 35-40 GPa with a double-sided LHDAC by rastering for ~20 minutes at a temperature between 2,000-2,300 K to minimize Soret diffusion to attain, at least, local equilibrium. The heating was steady throughout, both spatially and temporally, as is possible when using even thermal insulation layers (Du et al., 2015) and the use of homogeneous glass starting samples (i.e., no hot spots or flashing). The spot size of the laser (~30 μm) was smaller than the sample (~100 μm); therefore, we rastered the laser across the sample in order to convert the sample and to reduce horizontal temperature gradients. To maintain gasket stability, we avoided laser heating the edge of the gasket hole. The incident x-ray beam, ~5 x 7 μm in size, was centered on the converted samples. At each increase in pressure, up to 70-75 GPa, we additionally heated the sample for approximately 5 minutes to anneal the sample prior to room-temperature XRD. Additionally, we collected XRD upon samples quenched from both high pressures and high temperatures (Figure 2). Quenched samples were hand polished and compositions investigated in cross section by electron probe microanalysis (EPMA, Tables S3-S4). Compared with starting compositions (Tables S1, S2), the resulting compositions were found to agree (Table S5), in part due to the small grain sizes of the phases synthesized as compared to the electron beam size, thus averaging over phase(s) present (see Supporting Information: Section II).

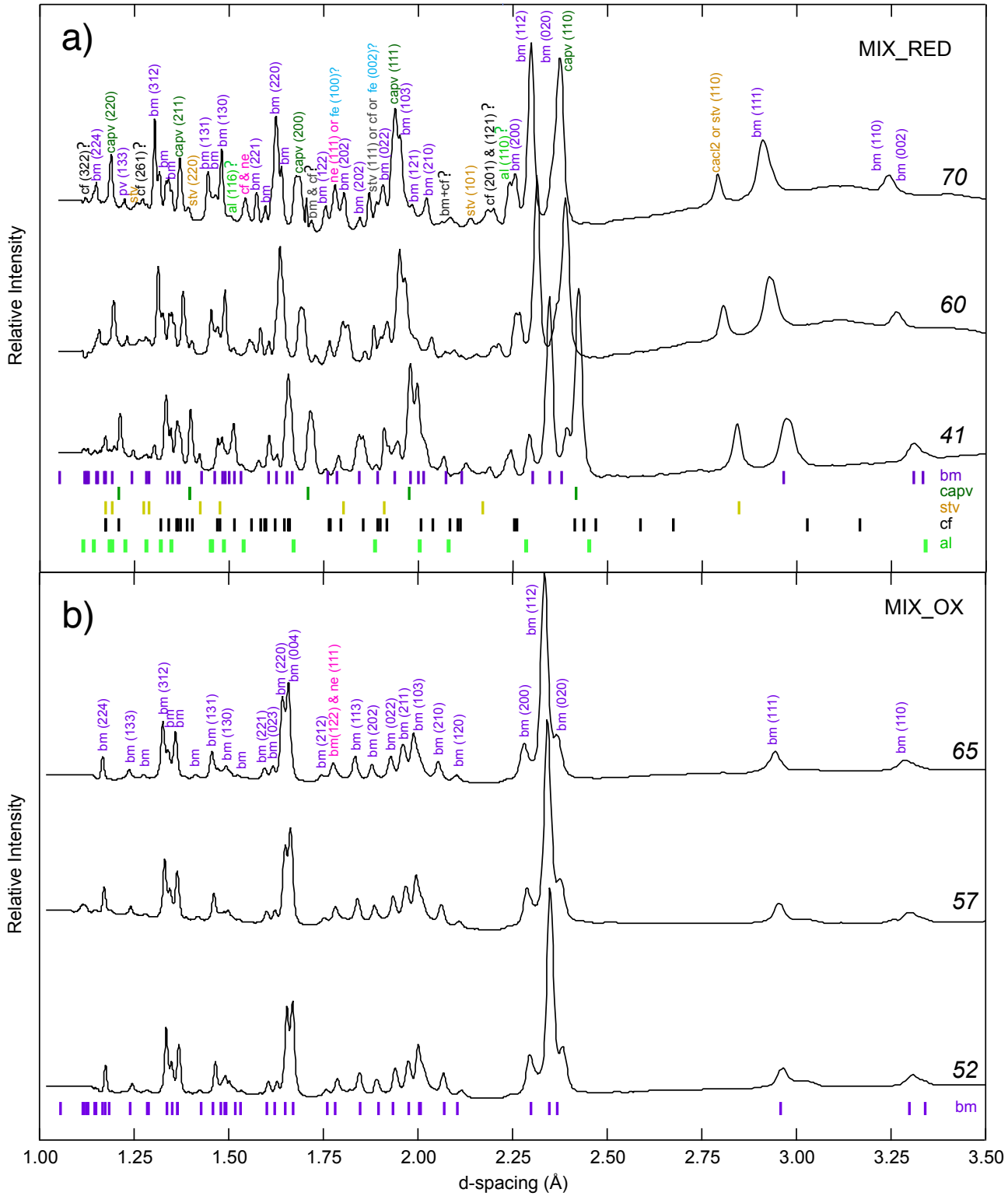

Figure 1. Selected quench XRD patterns with pressures given in GPa from the (**a**) reduced MIX_RED samples and (**b**) oxidized MIX_OX samples with present phases labeled as bridgmanite (bm), calcium perovskite (capv), stishovite (stv), calcium-ferrite structured phase (cf), alumina (al), neon (ne), and iron (ε-Fe). The peaks are labeled corresponding to the phase and *hkl* indices. See Figures S6 and S7 for representative Rietveld refined XRD patterns.

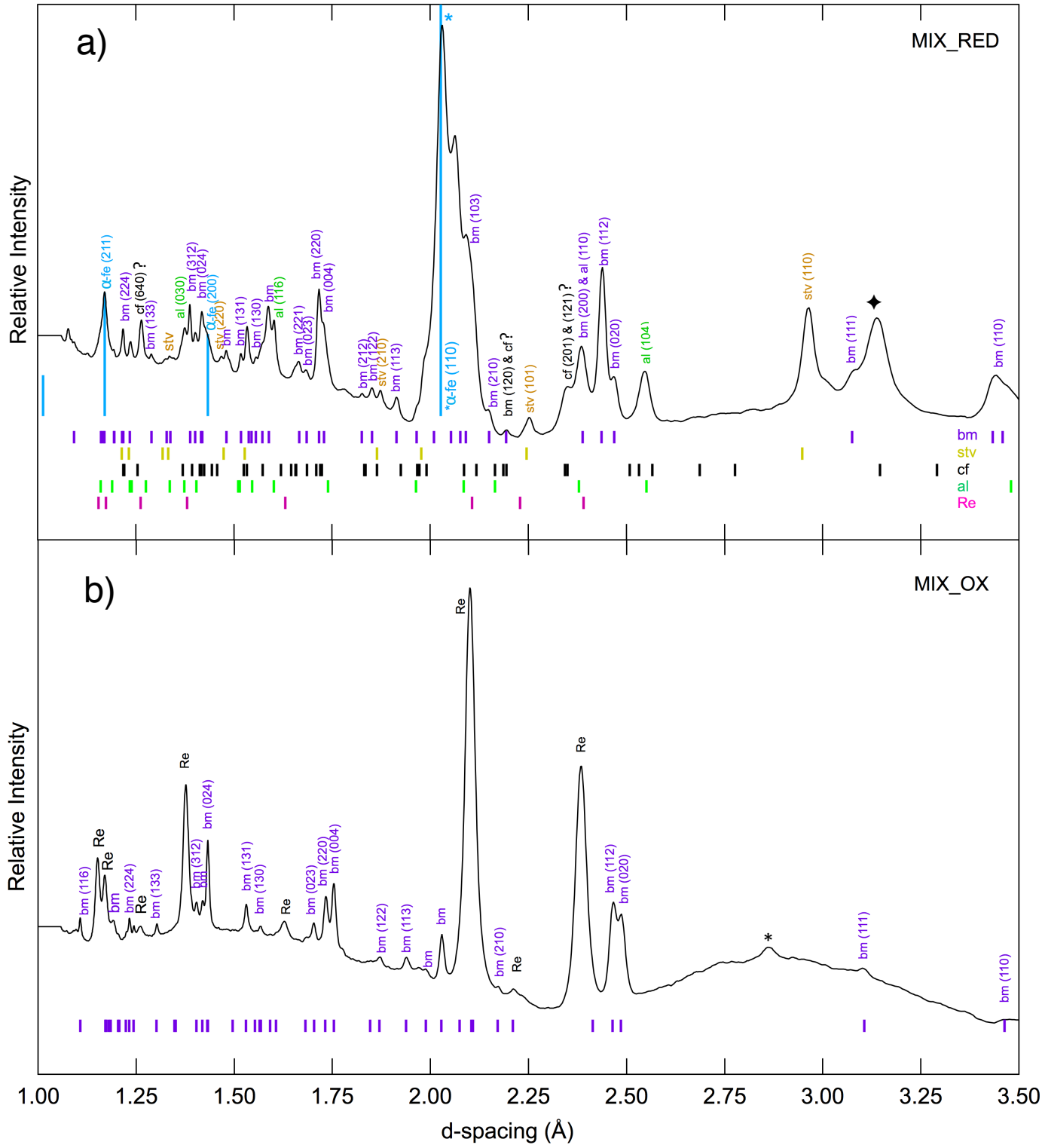

Figure 2. Room pressure and temperature XRD pattern for **(a)** MIX_RED and **(b)** MIX_OX with present phases labeled as bridgmanite (bm), stishovite (stv), calcium-ferrite structured phase (cf), alumina (al), rhenium (Re), and bcc iron (α-Fe). The peaks are labeled corresponding to the phase and *hkl* indices. ✦ This sample, a quenched sample held in its gasket and removed from the LHDAC, experienced blockage from the lead holder and this feature is due to the 100% line of lead which is offset from its usual d-spacing because of its different distance to the detector as compared to the sample-to-detector distance. *An anomalous peak that could not be assigned to the bridgmanite Pnma structure. The broad hump between ~2.5 – 3.5 Å and Re diffraction suggests that this pattern was collected near the edge of the gasket where the initially glass sample was unheated thus yielding an amorphous-like character.

Additionally, we used Monte Carlo modeling in order to fully explore the uncertainties from our measurements and deduce mineralogy and phase compositions of the assemblages synthesized under lower mantle conditions (Supporting Information: Section VI).

3 Results

3.1 X-ray Diffraction

3.1.1 MIX_RED Assemblage

X-ray diffraction of the more reduced composition MIX_RED shows a consistent mineralogy over every pressure step (Figure 1a). At lower mantle pressures, we observe bridgmanite (bm: (Mg, Fe, Al, Si)O_3), calcium silicate perovskite (capv: $CaSiO_3$), silica as stishovite (stv: SiO_2) or in the $CaCl_2$ structure, a calcium ferrite structured phase (cf: 20:80 solid solution between $MgAl_2O_4$ and $FeAl_2O_4$ calculated from Stixrude and Lithgow-Bertollini (2011)), possibly alumina (al: Al_2O_3), and possibly metallic iron (Fe). The first three phases: bridgmanite, calcium silicate perovskite, and silica have clear, distinct XRD peaks at all pressures, as marked in Figure 1a, whereas the remaining three phases are harder to identify by only XRD (see below). Common mantle phase ferropericlase (Mg,Fe)O was not observed in our experiments because the starting material has a molar (Mg+Fe)/Si < 1 (Table 1).

Bridgmanite, as expected, shows the most dominant XRD peaks (Figure 1a). The bm volumes are expanded from the Mg-endmember $MgSiO_3$, consistent with the expected inclusion of Fe and Al into the crystal structure (Andrault et al., 2001) (Figure 3). Al^{3+} and Fe^{3+} can be present on the A or B site of $MgSiO_3$, but Al^{3+} prefers the B site (Brodholt, 2000; Vanpeteghem et al., 2006). Therefore, when more Fe^{3+} is present, more Al^{3+} can be absorbed into bm. Since Al^{3+} and Fe^{3+} are present together in this sample, both expand the unit-cell volume, along with Fe^{2+}

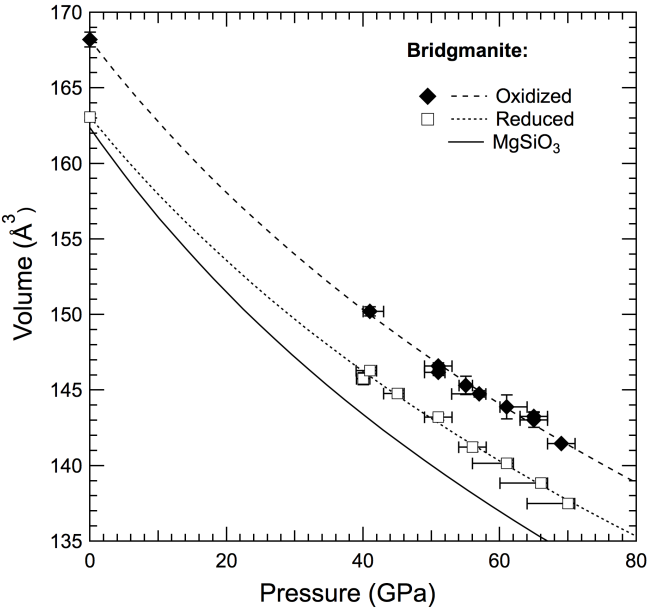

Figure 3. Pressure versus volume of bridgmanite at room temperature, with corresponding Birch–Murnaghan equation of state curves. MIX_RED (open squares, dotted curve) and MIX_OX (filled diamonds, dashed curve) samples are shown with pressures and their uncertainties are given by error bars (see Tables S6, S7). A solid curve is shown for pure endmember $MgSiO_3$ bm (Ballaran et al., 2012).

(Frost et al., 2004; Walter et al., 2006; Lundin et al., 2008; Hummer and Fei, 2012) (Figure S12).

At room temperature, calcium silicate perovskite shows the predicted tetragonal structure beginning at 50 GPa and above (Shim et al., 2000), shown as the capv peak splitting around the d-spacing for the (200) plane in Figure 1a. At high temperatures, we observe the capv structure reduces to the typical cubic structure and the peak splitting disappears. The volume of cubic capv follows closely to that measured previously, suggesting the composition is at or near the composition of pure $CaSiO_3$ (Mao et al., 1989) (Figure S4a). Calcium silicate perovskite becomes amorphous once quenched to room pressures and temperatures (Figure 2a) consistent with previous measurements (e.g., Mao et al., 1989; Tamai and Yagi, 1989; Shim et al., 2000; Ringwood and Major, 1971).

Because of the relatively high abundance of silicon in the starting composition (Table 1), silica is expected to be present, at least at a few percent, in the synthesized sample. Indeed, stishovite XRD peaks are readily visible due to the high symmetry of the phase and several of the peak positions situated away from the more dominant bridgmanite XRD peaks. The onset of the phase transition of stishovite (stv) to the $CaCl_2$ structure in silica (Dubrovinsky et al., 1997) appears to be present at pressures greater than 65 GPa, as we observe a slight volume contraction (Figure S4b).

The remaining phases (calcium ferrite, alumina, metallic iron) are much harder to identify at high pressures through XRD due to the combined effects of low abundance, symmetry, and overlap with the dominant bridgmanite and the higher symmetry phases (calcium perovskite and stishovite). The calcium-ferrite structured phase overlaps significantly with other phases at high pressures, but the (201) and (121) peaks are distinct from the other phases (Figure 1a), thus it is possible to determine volumes with a few more peaks (Figure S4c, Table S11). In addition, we

find that cf is required in the MIX_RED assemblage for charge balance of all elements. In the EPMA maps, we also find regions that are enriched with Fe and Al – indicative of Fe-rich cf phase (see Figure S8b in Supporting Information).

Similarly, alumina is not obviously apparent in the XRD patterns at high pressures due to the significant overlap with bridgmanite. However, the bridgmanite (200) peak appears to broaden at 60 GPa becoming two distinct peaks at 65 and 70 GPa, which we identify as the (110) peak of alumina, thus we are able to determine alumina volumes at the highest pressures conducted in this study (Figure S4d). In addition, alumina is possibly visible upon quenching to room conditions in XRD (Figure 2a) and EPMA (Figure 4, S11). However, we could not measure a reliable equation of state for alumina although the volumes measured are consistent with Jephcoat et al. (1988). We also consider the effect of no alumina forming in our Monte Carlo models (see section 3.3) and find that the formation of alumina is not completely necessary for charge balance to be maintained. Therefore, we model two variations on our possible assemblage: one model with the assumption of the formation of alumina (*Model A* in Supporting Information: Section VI) and the other without (*Model B* in Supporting Information: Section VI).

For metallic iron, the (100) plane of the hexagonal-close packed ε-Fe (Jephcoat et al., 1986) possibly shows itself in the XRD patterns at high pressure; however, its proximity to the strongest neon peak makes its presence ambiguous. However, upon quench to room conditions where Ne is no longer present due to evaporation, the low-pressure α-Fe phase shows strong diffraction intensity (Figure 2a). The volume of iron could only be reliably measured at room pressure: V_0 (23.64 ± 0.06 Å^3), which is within literature uncertainties (23.54 ± 0.05 Å^3 [Wilburn and Bassett, 1978]). Therefore, we also explore the formation of metallic iron in the Monte Carlo modeling as iron disproportionation, which occurs when Fe^{2+} self reduces to Fe^{3+} and metallic iron.

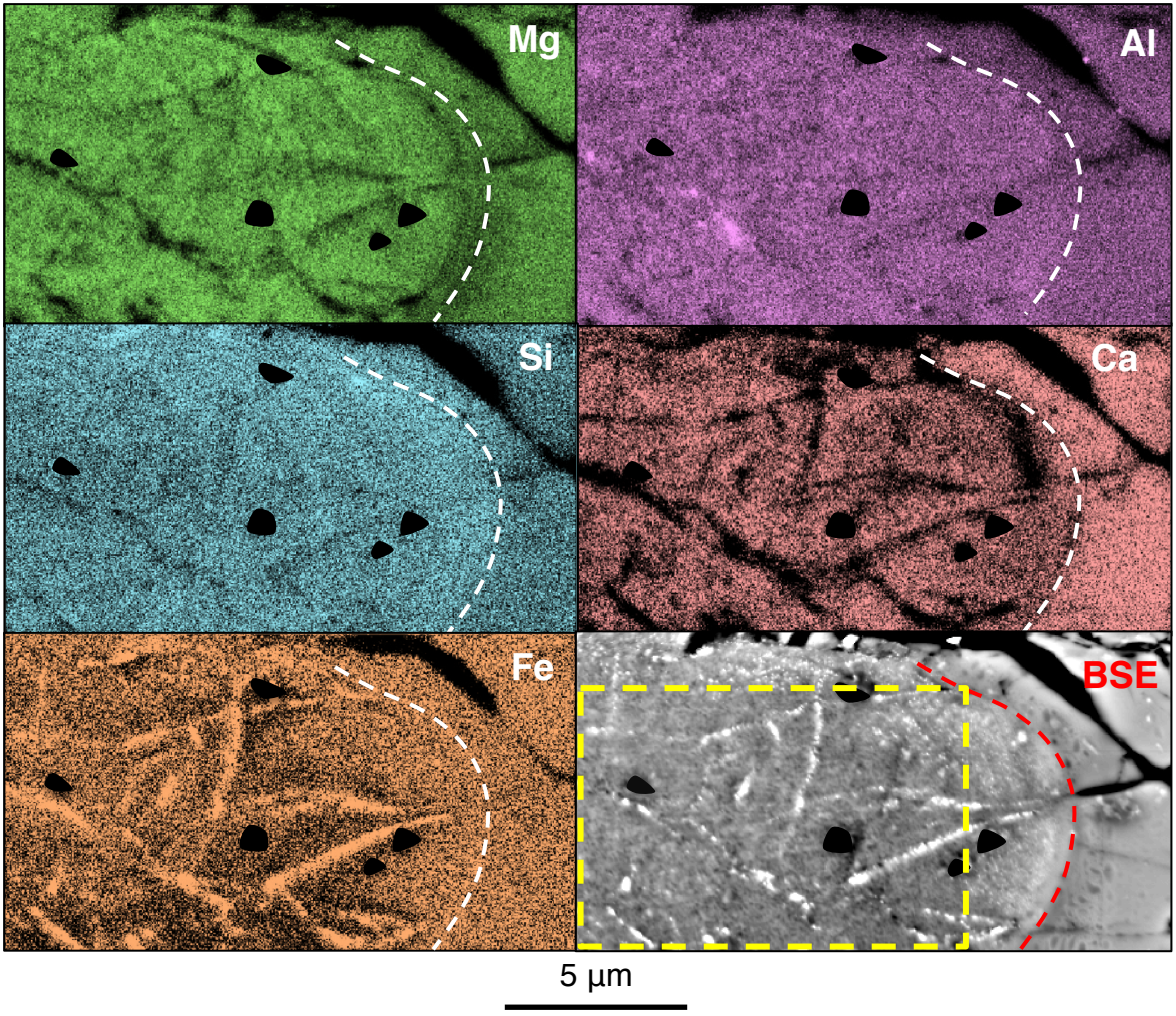

Figure 4. Backscattered secondary electron (BSE) image and elemental WDS mapping of Mg, Si, Fe, Al, and Ca of the quenched MIX_RED assemblage, hand-polished in cross-section. The reduced assemblage is quenched from 40 GPa and 2000 K. Note that the map has several areas showing elevated Fe and Al consistent with grains of metallic iron and alumina. The blacked-out regions denote dust on the surface of the sample and are removed from composition analyses. The dashed curve denotes the edge of the converted region within the sample. Everything to the right of the dashed curve is unconverted starting material (glass powder) that is adjacent to the edge of the gasket and unheated, while to the left of the dashed curve is the heated and converted sample. The yellow dotted box represents chemical analysis conducted in Supporting Information (Figure S8, S9, and S11).

To confirm our analysis of the phases present in the MIX_RED sample, we conducted a Rietveld refinement with GSAS-II (Toby & Dreele, 2013) on an XRD pattern shown in Figure 1a at 60 GPa (Supporting Information: Figure S6). The resulting refined volumes are nearly identical to values picked by hand, giving additional confidence to our determined phases and volumes (Figure 3; see Supporting Information: Tables S6, S8-S12, Figure S4).

3.1.2 MIX_OX Assemblage

In the oxidized sample, we observe only bridgmanite. No other phases were detected using XRD. Notably, the MIX_OX bridgmanite XRD peaks yield significantly expanded volumes from the Mg-endmember as well as the MIX_RED bm (Figures 3, S12), suggesting significant enrichment in cations other than Mg and Si (e.g., Catalli et al., 2011; Andrault, 2003). The quenched XRD pattern shows rhenium diffraction from the gasket and bridgmanite (Figure 2b). Bridgmanite appears to fit the traditional Pnma structure as reported in Tschauner et al. (2014).

To confirm our analysis of the phases present in the MIX_OX sample, we conducted a Rietveld refinement with GSAS-II (Toby & Dreele, 2013) on an XRD pattern shown in Figure 1b at 52 GPa (Supporting Information: Figure S7). The results of the refinement are nearly identical to our values picked by hand (Figure 3; see Supporting Information: Tables S7, S13).

3.1.3 Equations of State

We calculate the Birch-Murghangan 2nd-order equation of state (Birch, 1952) for bridgmanite for both sets of samples (Figure 3, Table 2), as well as compare unit-cell volumes of calcium perovskite, stishovite, calcium-ferrite structure, and alumina from the MIX_RED samples to equations of state from the literature (Figure S4). The MIX_OX bridgmanite volume is ~3%

larger than the MIX_RED bridgmanite. Since no capv is present, the expanded unit cell is likely to be due to the incorporation of Ca into the MIX_OX bridgmanite structure (Figure S12) (see natural bridgmanites in Tschauner et al., 2014). Additionally, the bulk moduli of the two bridgmanites are nearly identical, where both are ~12% stiffer than a pure $MgSiO_3$ bridgmanite (Table 2). All unit-cell parameters and volumes determined for Figures 3, 6 and S4 are listed in the Supporting Information (MIX_RED: Tables S8 – S12; MIX_OX: Table S13).

3.2. Electron Probe Microanalyses

Recovered samples were also examined by EPMA (see Supporting Information: Section II). The MIX_RED assemblage (Figure 4) generally agrees with the XRD results, showing areas possibly enriched in iron and aluminum, consistent with metallic iron and alumina XRD observations. Stishovite and calcium perovskite do not appear to show obvious regions enriched in silicon or calcium in the EPMA maps, which may be due to the relatively low abundance of stishovite and calcium perovskite becoming amorphous when quenched to room pressure and temperature.

The EPMA results of the oxidized recovered samples (Figure 5) reveal a nearly homogenous material with little variation in the distribution of elements. This is consistent with the XRD which suggests an assemblage that is dominated by a single phase, bridgmanite. There appears to be no variation in grain size or heterogeneity in the distribution of iron, indicating that the sample was well insulated from the anvils (Du et al., 2015; Sinmyo & Hirose, 2010). All EPMA results are listed in Tables S1-S5 in the Supporting Information. The maps in Figures 4 and 5 reflect WDS (wavelength-dispersive spectroscopy) measurements, while the raw data in Tables

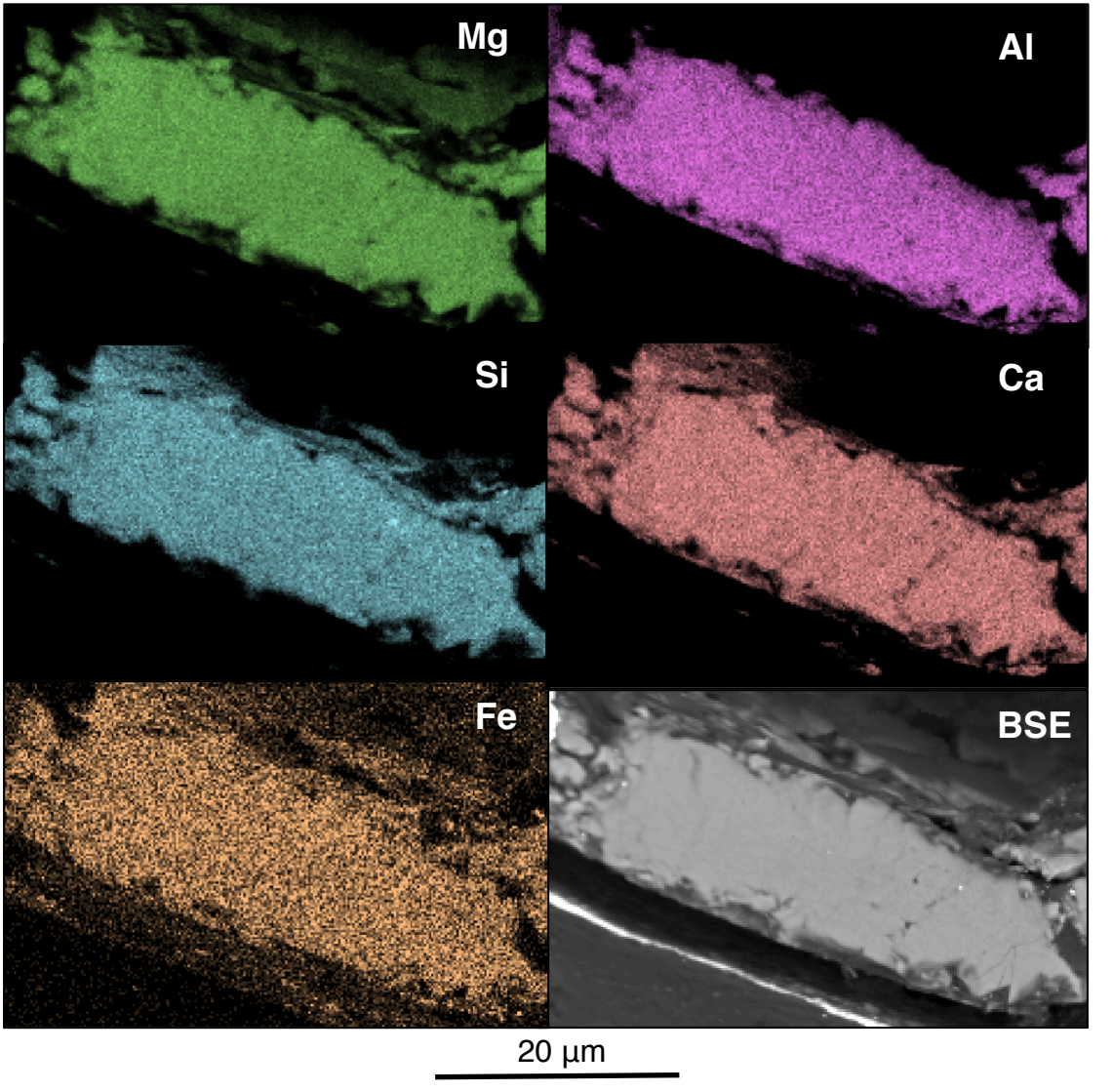

Figure 5. Backscattered electron SEM image and elemental WDS mapping of Mg, Si, Fe, Al, and Ca of the quenched MIX_OX assemblage, hand-polished in cross-section. The oxidized assemblage is quenched from 65 GPa and 2000 K. Note that the map is very homogenous across all elements.

S1-S5 are also WDS measurements. All data presented in Tables 1 and 3 are based on the WDS measurements.

3.3 Determining phase abundance in assemblage

3.3.1 MIX_RED Assemblage

The mineralogy of the two samples and composition of bridgmanite (Table 3) were determined by XRD (Figures 1, S6) and analysis of EPMA point measurements and element maps via Monte Carlo modeling and mass/charge balance. We use Monte Carlo modeling since XRD intensities are an imperfect tool to constrain composition robustly as texture and backgrounds in LHDAC experiments can be significant, thus, making it difficult to pull out phase abundance from XRD intensities alone (e.g., measurement techniques and preferred orientation: McCusker et al., 1999). In order to determine the molar abundance of each phase, additional information and assumptions are necessary beyond mass balance. In the MIX_RED samples, we observe bridgmanite, calcium perovskite, stishovite, and potentially a calcium ferrite structured phase, alumina, and metallic iron (these are free parameters in the modeling); however, we could not uniquely identify the exact percentages of each mineral since the solutions are non-unique. Using image-processing on the MIX_RED sample composition maps (Figure 4 and Figure S9), we infer the bright spots on the backscattered electron image are possibly metallic iron. Additionally, metallic iron formation cannot exceed 0.7 mol% (corresponding to ~0.18 vol%) because of limitations on how much ferric iron can form within this sample based on Monte Carlo modeling (Figure S13). Therefore, this sample may consist of six independent phases and is derived from six starting oxides: FeO, Fe_2O_3, MgO, SiO_2, CaO, and Al_2O_3, hence our synthesized samples do not violate the thermodynamics phase rule.

To estimate the approximate amounts of each material, we conducted Monte Carlo modeling (see Supporting Information: Section VI), where we sampled each unknown variable as a uniform distribution. Our unknown variables are the following: the distribution of aluminum between alumina and bridgmanite, the distribution of silicon between stishovite and bridgmanite, the distribution of magnesium between calcium ferrite and bridgmanite, the distribution of Fe^{2+} between calcium ferrite and bridgmanite, and how much iron disproportionated. We performed the search with the following assumptions that performed as cutoffs for acceptable chemical compositions for the first model where we assume all of the minerals we have discussed are present (*Model A*): (1) each mineral is charge balanced; (2) self-reduction of iron may have occurred (the Fe^{3+} content changed during the experiment from the initial starting value following the reaction: $3xFe^{2+} \rightarrow 2xFe^{3+} + xFe^{0}$ where $0 < x \leq 1$) for the MIX_RED samples since metallic Fe may be present at low levels in XRD (Figure 2) and EPMA measurements (Figure 4); (3) calcium perovskite phase is the only calcium-bearing phase for the MIX_RED samples; (4) the calcium-ferrite structured phase is a solid solution between $MgAl_2O_4$ and $FeAl_2O_4$; (5) use the measured bridgmanite V_0 and existing literature to estimate volume expansion due to cation incorporation (see Supporting Information: Section VI); and (6) assume all Fe^{3+} is incorporated into the bridgmanite structure. We also conduct a second Monte Carlo model (*Model B*), which is similar to *Model A* with two important exceptions: we exclude the disproportionation of iron and exclude alumina formation. With these constraints, we modeled several possible mineral assemblages and their uncertainties (Table 3).

The Monte Carlo results indicate that there are many tradeoffs between the different unknown variables. The following discusses the results of *Model A*, which assumes all minerals present. For example, how Fe and Mg partitions between cf and bm is unknown; therefore, the cf

content in the MIX_RED assemblage can vary from 10 to 20 mol% (Table 3). With our assumptions and wide constraints, we can robustly constrain the bm content to be between 42 and 53 mol%. Approximately 5 mol% of the bm structure contains other cations not present in the pure $MgSiO_3$ unit cell; such as Al, Fe^{2+}, and Fe^{3+}, with their relative abundance primarily constrained from the unit-cell volume at room conditions V_0 (Figure S12). Based on 6,000 successful runs out of 500 million Monte Carlo runs using assumptions 1-7 of *Model A*, the mean values of the phases present in the assemblage are as follows in mol%: bm (50%), capv (18%), cf (12%), al (9%), stv (9%), and metallic Fe (0.2%). Averaging over all runs, the cf phase likely consists of a 20:80 mixture of $MgAl_2O_4$ and $FeAl_2O_4$ but can vary from 7:93 to 50:50 (see Figure S4c). In addition, metallic iron does not necessarily need to form to fit all of our data constraints. While metallic iron could exist up to 0.7 mol%, the maximum probability is between 0 and 0.2 mol%.

For *Model B* (no alumina or metallic iron formation), we calculate mineralogical assemblages that are more tightly constrained. The mean values of each phase present are as follows in mol%: bm (40.5%), capv (18.4%), cf (22.7%), and stv (18.4%). Averaging over all runs, the cf phase likely consists of a 50:50 mixture of $MgAl_2O_4$ and $FeAl_2O_4$. Full details on the Monte Carlo modeling can be found in the Supporting Information: Section VI. Model B is consistent with a previous study, that performed thermodynamic calculations on a pyroxenite composition, which yielded a mineral assemblage of bridgmanite, calcium perovskite, calcium ferrite, and stishovite phases (Adam et al., 2017).

3.3.2 MIX_OX Assemblage

For the MIX_OX samples, we only identified bridgmanite by XRD (Figures 1-2, S7). We do not observe the decomposition of bridgmanite in the oxidized sample at quench. It remains as a single bm phase throughout compression and decompression.

To determine the composition of bridgmanite, we used the EPMA results (Table 1) and conducted a mass balance calculation with the following assumptions: (1) no change in the Fe^{3+} content from the initial starting material as we do not observe any metallic iron in the synthesized assemblage (however, it may be possible that Fe^{3+} content may have changed due to other causes that we do not consider [Lauterbach et al., 2000]); (2) use the measured V_0 and existing literature to estimate volume expansion due to cation incorporation (see Supporting Information: Section VI, Figure S12); and (3) calcium is allowed to exist in solid solution with bm since capv is not observed in XRD. The resulting bridgmanite composition is given in Table 3. Because of the large V_0 measured for MIX_OX bridgmanite, Ca was allowed to enter the bridgmanite structure since the iron and aluminum present in the starting material is not enough to increase V_0 to the observed V_0 (Figure S12). As such, we used a linear interpolation with the volume of capv as four times its normal cubic volume (i.e., 181.48 $Å^3$) to account for the difference in the number of atoms between capv (5 atoms) and bm (20 atoms) (Andrault, 2003). This bridgmanite composition contains a large fraction of cations (~38%) other than Mg and Si. This is in contrast to the bm in the MIX_RED samples where the cation concentration that is not Mg or Si is only ~5%. We posit that Ca^{2+} replaces Mg^{2+}, similar to the way Fe^{2+} replaces Mg^{2+} on the A-site (Tschauner et al., 2014). More research is required to investigate which site calcium prefers.

We also considered other possible calcium-bearing minerals that could explain the lack of $CaSiO_3$ calcium perovskite. If calcium perovskite is present in this sample, it would be in much smaller quantities (< 5%) compared to the MIX_RED samples, such that it would be difficult to

observe in the x-ray diffraction. In addition, if there is an unknown phase hosting calcium (e.g., calcium oxide [CaO], calcium aluminate [$CaAl_2O_4$]) it would have to also be in low abundance or low symmetry compared to bridgmanite such that it is not observed with XRD or EPMA. Therefore, while we lack the precision to confirm a Ca-bearing bridgmanite, the volumes measured are consistent with such a phase and with the lack of any other kind of Ca-bearing phases in this sample, despite the high abundance of Ca in the starting material (Table 1). Future work will require more detailed analyses of this sample to confirm Ca-bearing bridgmanite, such as single-crystal x-ray diffraction or transmission electron microscopy.

4 Discussion

The difference in mineralogy between the two samples can be explained by the large contrast in Fe^{3+} content. We infer that the higher amount of Fe^{3+} in the oxidized sample encourages the incorporation of more Al^{3+} cations into the bridgmanite structure by charge-coupled substitution (Navrotsky et al., 2003), which leads to a more expanded bridgmanite volume. However, the expanded unit-cell volume for bridgmanite in the oxidized sample is larger than expected if only iron and Al^{3+} are incorporated (O'Neill and Jeanloz, 1994; Walter et al., 2006) (Figure S12). Therefore, since there is no XRD observation of calcium perovskite, we infer that calcium has also been incorporated into the bridgmanite structure, a likelihood made possible by an already expanded unit cell provided by the large amounts of iron and Al^{3+} (Jung & Schmidt, 2011). We expect Ca would be present on the Mg site, due to the charge of calcium, Ca^{2+}. The addition of Ca into the bridgmanite structure further increases the unit-cell volume, consistent with the larger volume measured for the MIX_OX samples (Figure 3). While many studies have reported a large miscibility gap between $MgSiO_3$ bridgmanite and $CaSiO_3$ perovskite (e.g.,

Armstrong et al., 2012; Irifune et al., 1989; Jung and Schmidt, 2011; Tamai and Yagi, 1989), the combined effect of Al and Fe^{3+} on the solubility of bridgmanite and calcium perovskite were beyond the scope of those studies. We posit that the inclusion of high amounts of Al and Fe^{3+} enhances the solubility of Ca into bridgmanite, decreasing the miscibility gap. This result is consistent with a previous study which produced a bridgmanite with comparable amounts of calcium although a V_0 was not reported (Miyajima et al., 1999). The bridgmanite formed in Miyajima et al. (1999) also contained large amounts of Al^{3+} (19%, compared to our 23%) and estimated the Fe^{3+} content to be approximately ~83% $Fe^{3+}/\Sigma Fe$ (based on charge balance of bridgmanite), thus consistent with our high ferric iron content. It is likely that there is a threshold of Al, Fe^{2+}, and Fe^{3+} content that must be met before Ca is soluble in bridgmanite in appreciable amounts, warranting further study. As most studies do not list their ferric iron content, it is difficult to constrain the necessary amounts of Al and Fe^{3+} required for the closing of the miscibility gap. Given our sample compositions, we can only constrain the threshold to between 11% and 55% $Fe^{3+}/\Sigma Fe$ with an assemblage with 8% FeO and 13% Al_2O_3. More work is needed to fully understand where the miscibility gap closes for bridgmanite and calcium perovskite given the combined effects of Al, Fe^{2+} and Fe^{3+} (e.g., Jung and Schmidt, 2011).

A typical Mg-silicate bridgmanite crystallizes in the distorted orthorhombic Pnma structure with unit-cell axial ratios of a:b:c ~ 1:1:$\sqrt{2}$ (Catalli et al., 2011). As such, we can track the axial ratios, b/a (~1) and c/a (~$\sqrt{2}$), versus pressure to observe how the distortion changes (Figure 6). As pressure increases, the b/a axial ratios increase linearly for both MIX_OX and MIX_RED samples, albeit at different rates. However, the c/a ratios behave in a more unusual way: the MIX_RED ratios increase linearly with pressure, while the MIX_OX ratios are more quadratic in shape, similar to what has been reported previously (as summarized by Catalli et al., 2011). Since

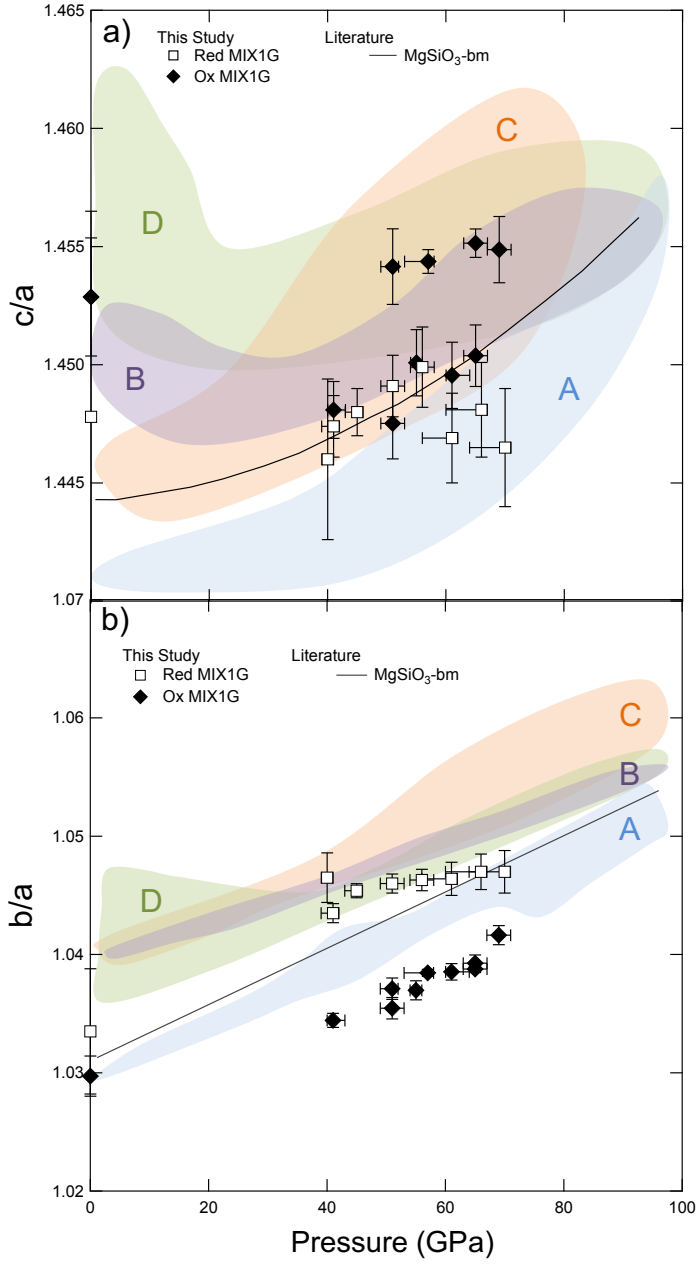

Figure 6. Axial ratios of bridgmanite, **(a)** b/a and **(b)** c/a, with different compositions. Squares: MIX_RED bridgmanite (this work), diamonds: MIX_OX bridgmanite (this work), solid line: bridgmanite (Ballaran et al., 2012). Shaded regions denote compositions listed in Table 2: blue (A): Fe^{2+}-bearing bridgmanite; purple (B): Fe^{3+}Al-bearing bridgmanite; orange (C): Fe^{3+}-bearing bridgmanite; and green (D): Al-bearing bridgmanite.

438 the MIX_RED bridgmanite has a mixture of Fe^{3+}, Fe^{2+}, and Al^{3+}, the axial distortions fall between
439 the expected distortions of various other bridgmanites with different compositions. The axial ratios
440 of the MIX_OX bridgmanite shows the *b* and *a* axes are distorted much more than other
441 compositions of bridgmanite, likely due to the incorporation of Ca^{2+} in the Mg-site.
442
443 **4.1 Implications for Lower Mantle**
444 To understand the effects on the bulk sound velocity and density of each mineral
445 assemblage, we calculated these values with the Burnman toolkit (Cottaar et al., 2014) using our
446 experimentally determined values of the equations of state of the respective bridgmanites (Table
447 2), a mantle geotherm (Brown & Shankland, 1981), our computed phase abundance and
448 composition (Table 3), and existing literature values for the other phases based on Stixrude and
449 Lithgow-Bertelloni (2011) (Figures S4). We considered other geotherms as well, but there is no
450 effect on the relative difference between the reduced and oxidized samples' density and seismic
451 velocities, just an effect on their absolute magnitude which is important when comparing to
452 seismological models. We also do not consider the spin transition of iron, which is beyond the
453 scope of this study. In order to properly treat the cf composition, we explored the entire range of
454 possible compositions of cf assuming a solid solution between $MgAl_2O_4$ and $FeAl_2O_4$ for
455 MIX_RED (as discussed in Supporting Information: Section III). Therefore, we applied solid
456 solution mixing using Stixrude and Lithgow-Bertollini (2011). For capv, there is some
457 disagreement between equations of state, where our measured volumes differ from the capv
458 equation of state of Stixrude and Lithgow-Bertelloni (2011). As such, we fit a 2^{nd}-order Birch-
459 Murnaghan equation of state to our measured capv volumes holding V_0 fixed (45.58 $Å^3$; Shim et
460 al., 2000) yielding a room-pressure, room-temperature bulk modulus K_0 of 260 (±10) GPa. Figure

S5 illustrates the small effect the chosen capv equation of state has on density (< 0.3%) and the bulk sound speed (< 0.9%) of the MIX_RED assemblage.

The resulting assemblages of the two samples yield the MIX_RED assemblage to be slightly denser than PREM by ~1% at the top of the lower mantle even when considering multiple temperature profiles of the mantle (Anderson, 1981; Brown & Shankland, 1981; Ono, 2008; Stacey & Davis, 2008) (Figure 7). At the bottom of the mantle, the MIX_RED assemblage density is similar to that of PREM. The thickness of each line in Figure 7 encompasses the entire set (both *Models A* and *B*) of possible densities and bulk sound speeds with 95% confidence for MIX_RED. MIX_OX assemblage leads to larger seismic velocities than the reduced MIX_RED assemblage and PREM mainly due to the large differences in bulk moduli of the secondary phases in MIX_RED. Based on these results, Fe^{3+} has a strong effect on the whole rock mineralogy and resulting density and seismic properties of the assemblage.

In addition, if pyroxenite (in a reduced or oxidized state) exists within the lower mantle, then pyroxenites would be viewed as positive seismic anomalies (bulk sound speed) on the order of 4-7% as compared to PREM. However, pyroxenites encompass a wide class of compositions (Figure S3); therefore, these seismic speed differences may differ between pyroxenite assemblages. More work is required on the various pyroxenite assemblages and how redox impacts mineralogy to fully understand potential sources of seismic anomalies. Since our samples are aluminum rich, a more aluminum-poor pyroxenite would result in less cf and alumina and increase the bridgmanite content. We predict that seismic wave speeds of Al-poor pyroxenites would be faster since the bridgmanite content would increase.

When considering bridgmanite alone, MIX_RED bm does not differ significantly from $MgSiO_3$ when considering density (±1% difference); however, since the bulk modulus increases

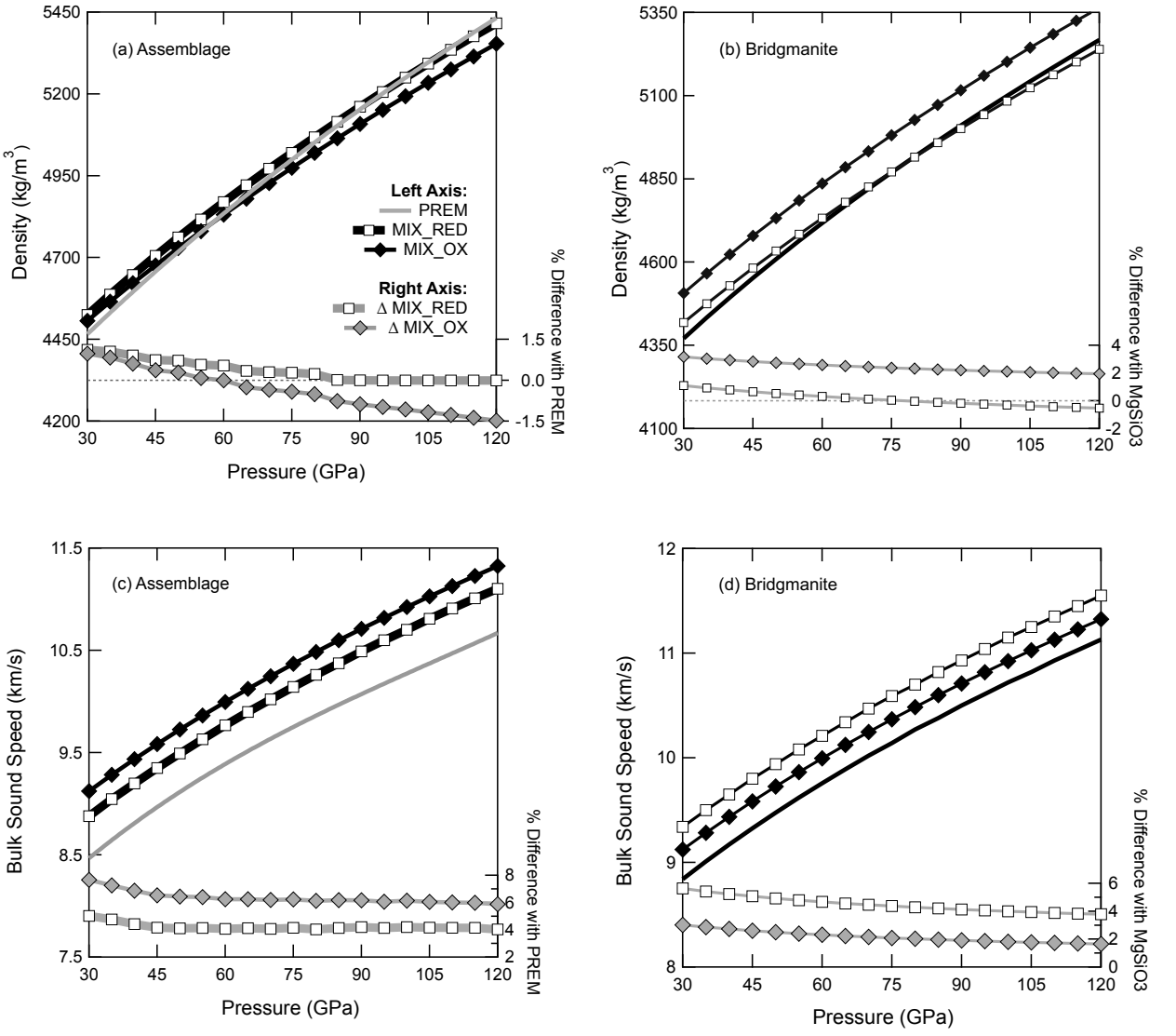

Figure 7. Computed assemblage density as computed by BurnMan (Cottaar et al., 2014) using the assemblages tabulated in Table 3 and using four different temperature profiles. (**a**) Density of 95% confidence of all possible MIX_RED assemblages (white squares) based on Monte Carlo results of *Models A* and *B* and MIX_OX assemblage (black diamonds) are plotted with PREM (thick gray curve) as reference. All possible densities are within the thickness of each corresponding line and consider four different temperature profiles: Stacy and Davis 2008; Ono 2008; Anderson et al., 1982; Brown and Shankland 1981. The right axis illustrates the percent difference of each sample with PREM (gray). (**b**) Computed assemblage bulk sound speed as computed by BurnMan with the same constraints as (**a**). (**c**) Density of 95% confidence interval for each synthesized bridgmanite from MIX_RED (white squares) and MIX_OX (black diamonds) as compared to pure bridgmanite, $MgSiO_3$ (black solid line). All labels are consistent with (**a**), but Brown and Shankland (1981) is applied here. Percent difference illustrates the difference between the bridgmanites synthesized in this study with pure bridgmanite (gray). (**d**) Computed bulk sound speed of bridgmanites from this study and pure bridgmanite. Constraints are the same as (**c**).

484 when bm includes impurities, the bulk sound speed of bm is greater than $MgSiO_3$ by ~1.7-3%
485 (Figure 7). MIX_OX bm is denser than the MIX_RED bridgmanite and $MgSiO_3$ despite the large
486 increase in unit-cell volume. The addition of impurities, such as Ca, dramatically increases the
487 density by ~2-3% as compared to $MgSiO_3$. MIX_OX bm also results in faster bulk sound speeds
488 (2-3%) as compared with $MgSiO_3$.

489 Previous work on the enstatite chondrite lower mantle composition (Javoy, 1995) shows
490 that increased ferric iron content decreases the density of the entire assemblage (Gu et al., 2016).
491 Our study is consistent with those findings with the reduced assemblage denser than the oxidized
492 assemblage, especially when considering the MIX_OX starting composition molar mass is greater
493 than MIX_RED by ~1.8% (Table 1). While the samples tested here do not reflect the bulk of the
494 lower mantle, these samples do show that when two compositions have different ferric iron
495 concentrations in the lower mantle, the resulting mineralogy (and density) can be quite different.
496 Other candidate lower mantle assemblages may also be affected by ferric iron content, where a
497 change in ferric iron content (not necessarily a change in bulk composition) can lead to changes in
498 mineralogy, thus, influencing assemblage seismic velocities and density, but other assemblages
499 require further study under more oxidizing conditions. Therefore, Fe^{3+} could induce mineralogical,
500 density, and/or velocity changes depending on the composition of the rock assemblage on the order
501 of a percent, creating lateral heterogeneity as viewed in seismic tomography without changing bulk
502 composition (French & Romanowicz, 2015), but more work is required to see the full effects of
503 Fe^{3+} on other compositions and for other Fe^{3+} contents. Of course, lateral heterogeneity apparent
504 in seismic tomography studies may also be evidence of a change in bulk composition, the presence
505 of volatiles and/or presence of melt as has been previously reported (e.g., Ohtani & Maeda, 2001;
506 Ono et al., 2001).

Another potential implication of this work is the apparent solid solution of bridgmanite with calcium perovskite. If calcium perovskite and bridgmanite is miscible in some cases (i.e., high Fe^{3+} and Al content), then a Ca-rich bridgmanite would be negatively buoyant compared to $MgSiO_3$ and other Fe, Al-rich bridgmanites (see Figure 7c). The effects on seismic speeds is more complicated since recent work has shown that Fe^{3+} can affect the shear modulus of bridgmanite (Kurnosov et al., 2017). Based on our work, bulk sound speed would be faster for a Ca-bearing bridgmanite compared to $MgSiO_3$, but not necessarily for Fe, Al-rich bridgmanites. Fe and Al stiffen bridgmanite, increasing the bulk modulus. However, since Ca also has an effect on bulk modulus, the increased density lowers the bulk sound velocity difference (see Figure 7d). In order to understand the full impacts on Ca-bearing bridgmanite seismic speeds, measurements of the shear modulus and/or seismic wave speeds are required. Because we do not have measurements of the shear modulus for our samples nor are they well constrained for the compositions of our samples, we do not present assemblage or bridgmanite compressional or shear velocities, v_p or v_s, respectively. However, given what we know about the shear modulus of endmembers $MgSiO_3$, $CaSiO_3$ and the other phases, we find that v_p and v_s for MIX_RED assemblage are also slower than MIX_OX.

While a Ca-rich bridgmanite may be rare in the mantle, if it exists, it may be able to incorporate other large-ion lithophile elements (LILE) such as uranium, thorium and potassium, important heat-producing elements in the deep mantle (Corgne & Wood, 2002). While Ca is rarely ever expected to form a solid solution with pure endmember $MgSiO_3$ due to Ca's large ionic radius, Fe^{3+} and Al^{3+} may be able to allow Ca into the bridgmanite structure. Other LILE have similar radii to Ca and may just as easily fit into the bridgmanite structure (Kesson et al., 1995).

5 Conclusion

We find that the crystal chemical behavior of iron in bridgmanite varies under different redox conditions thereby influencing mineralogy, density, and seismic velocities for this given pyroxenite composition. The samples presented here suggest that redox conditions may affect mantle mineralogy in the lower mantle; therefore, lateral variations in Fe^{3+} in the lower mantle could cause variations in seismic velocities and density given otherwise similar Al-rich pyroxenite compositions. Our experiments illustrate that Fe^{3+} and possibly Al content can have a profound effect on the formation of Ca-bearing bridgmanite, secondary mineral formation, density, and changes in seismic speeds. These results along with previous work on enstatite chondrites (Gu et al., 2016) show that Fe^{3+} may have a similar impact on other compositions at lower mantle conditions. In general, a more oxidized Al-rich pyroxenite sample (high $Fe^{3+}/\Sigma Fe$), yields a simpler assemblage of bridgmanite and faster seismic bulk sound speeds (6 to 7%) and a similar density (1 to -1.5%) to PREM. In contrast, the reduced Al-rich pyroxenite sample yields a complex assemblage that is denser and slower than its oxidized counterpart. Additionally, we find that high Fe^{3+} content in our Al-rich pyroxenite samples stunts the formation of calcium perovskite and other oxides because a change in oxidation state of iron dramatically affects how cations are incorporated into the bridgmanite structure. Under oxidizing conditions, the miscibility gap between calcium perovskite and bridgmanite appears to disappear, at least for high Fe^{3+} and Al content, allowing for a sample consisting of Ca-bearing bridgmanite.

We predict that Ca-rich bridgmanite may form in regions of the mantle that are highly oxidizing and rich with Al, perhaps within subducted slabs. The implications of varying amounts of ferric iron could be far reaching, although other potential mantle lithologies should be further studied under varying redox conditions under lower mantle conditions to determine if this

553 phenomenon is universal. While pyroxenite may only exist in the lower mantle in low
554 concentrations, this study highlights the importance of investigating ferric iron effects on a variety
555 of mantle compositions, since ferric iron has been shown to have immediate implications on two
556 compositions under lower mantle conditions: an Al-rich pyroxenite (this study) and enstatite
557 chondrite lower mantle composition model (Gu et al., 2016). While there are several possible
558 compositional models of the lower mantle, bridgmanite is considered to be the dominant phase;
559 consequently, its crystal chemical behavior has a leading role in shaping the mantle's
560 thermochemical evolution.

561 **Acknowledgments, Samples, and Data**

562 We thank R. Weber and S. Tumber for glass synthesis; E. E. Alp and W. Bi for Mossbauer
563 measurements; S. Karato for discussions; Z. Jiang and J. Deng for technical support. We
564 thank the staff and beamline scientists at HPCAT in particular, Yue Meng and S. Tkachev for Ne
565 gas loading. This work was funded by an NSF CAREER grant to K.K.M.L. (EAR-0955824). N.C.
566 is supported by an NSF Graduate Research Fellowship DGE-1122492. EPMA was funded by the
567 NSF (EAR-0744154) and Yale University. Portions of this work were performed at GSECARS
568 (NSF EAR-1128799, DOE DE-FG02-94ER14466, and NSF EAR 11-57758 for the
569 GSECARS/COMPRES gas loading system), and HPCAT (DE-NA0001974, DE-FG02-
570 99ER45775, with partial instrumentation funding by NSF). This research used resources of the
571 Advanced Photon Source; a US DOE Office of Science User Facility operated for the DOE Office
572 of Science by ANL under Contract No. DE-AC02-06CH11357. K.K.M.L.'s effort partially
573 supported under the auspices of the U.S. Department of Energy by Lawrence Livermore National
574 Laboratory under Contract DE-AC52-07NA27344. All data included in the Supporting
575 Information, x-ray diffraction, and EPMA data analysis are included in the Mendeley data
576 repository (DOI: 10.17632/hj3wg6s7yd.2). We also thank the contributions and feedback from
577 two anonymous reviewers.

578

579 **References**

580 Adam, C., Caddick, M. J., & King, S. D. (2017). Pyroxenite causes fat plumes and stagnant
581 slabs. *Geophysical Research Letters*, 2017GL072943.
582 https://doi.org/10.1002/2017GL072943
583 Akahama, Y., & Kawamura, H. (2006). Pressure calibration of diamond anvil Raman gauge to
584 310GPa. *Journal of Applied Physics*, *100*(4), 043516. https://doi.org/10.1063/1.2335683
585 Anderson, O. L. (1981). Temperature Profiles in the Earth. In *Evolution of the Earth* (pp. 19–27).
586 American Geophysical Union (AGU). https://doi.org/10.1029/GD005p0019
587 Andrault, D., Muñoz, M., Pesce, G., Cerantola, V., Chumakov, A., Kantor, I., Pascarelli, S.,
588 Rüffer, R., & Hennet, L. (2018). Large oxygen excess in the primitive mantle could be
589 the source of the Great Oxygenation Event. *Geochemical Perspectives Letters*, 5–10.
590 https://doi.org/10.7185/geochemlet.1801
591 Andrault, D. (2003). Cationic substitution in MgSiO3 perovskite. *Physics of the Earth and*
592 *Planetary Interiors*, *136*(1), 67–78. https://doi.org/10.1016/S0031-9201(03)00023-2
593 Andrault, D., Bolfan-Casanova, N., & Guignot, N. (2001). Equation of state of lower mantle
594 (Al,Fe)-MgSiO3 perovskite. *Earth and Planetary Science Letters*, *193*(3), 501–508.
595 https://doi.org/10.1016/S0012-821X(01)00506-4
596 Armstrong, L. S., Walter, M. J., Tuff, J. R., Lord, O. T., Lennie, A. R., Kleppe, A. K., & Clark,
597 S. M. (2012). Perovskite Phase Relations in the System CaO–MgO–TiO2–SiO2 and
598 Implications for Deep Mantle Lithologies. *Journal of Petrology*, *53*(3), 611–635.
599 https://doi.org/10.1093/petrology/egr073
600 Ballaran, T. B., Kurnosov, A., Glazyrin, K., Frost, D. J., Merlini, M., Hanfland, M., & Caracas,
601 R. (2012). Effect of chemistry on the compressibility of silicate perovskite in the lower

602 mantle. *Earth and Planetary Science Letters*, *333*, 181–190.
603 https://doi.org/10.1016/j.epsl.2012.03.029
604 Birch, F. (1952). Elasticity and constitution of the Earth's interior. *Journal of Geophysical*
605 *Research*, *57*(2), 227–286. https://doi.org/10.1029/JZ057i002p00227Brodholt, J. P.
606 (2000). Pressure-induced changes in the compression mechanism of aluminous
607 perovskite in the Earth's mantle. *Nature*, *407*(6804), 620-622.
608 Brown, J. M., & Shankland, T. J. (1981). Thermodynamic parameters in the Earth as determined
609 from seismic profiles. *Geophysical Journal International*, *66*(3), 579–596.
610 https://doi.org/10.1111/j.1365-246X.1981.tb04891.x
611 Catalli, K., Shim, S.-H., Prakapenka, V. B., Zhao, J., & Sturhahn, W. (2010). X-ray diffraction
612 and Mössbauer spectroscopy of Fe3+-bearing Mg-silicate post-perovskite at 128–138
613 GPa. *American Mineralogist*, *95*(2–3), 418–421. https://doi.org/10.2138/am.2010.3352
614 Catalli, Krystle, Shim, S.-H., Dera, P., Prakapenka, V. B., Zhao, J., Sturhahn, W., Chow, P.,
615 Xiao, Y., Cynn, H., & Evans, W. J. (2011). Effects of the Fe3 + spin transition on the
616 properties of aluminous perovskite—New insights for lower-mantle seismic
617 heterogeneities. *Earth and Planetary Science Letters*, *310*(3–4), 293–302.
618 https://doi.org/10.1016/j.epsl.2011.08.018
619 Corgne, A., & Wood, B. J. (2002). CaSiO3 and CaTiO3 perovskite-melt partitioning of trace
620 elements: Implications for gross mantle differentiation. *Geophysical Research Letters*,
621 *29*(19), 1933. https://doi.org/10.1029/2001GL014398
622 Cottaar, S., Heister, T., Rose, I., & Unterborn, C. (2014). BurnMan: A lower mantle mineral
623 physics toolkit. *Geochemistry, Geophysics, Geosystems*, *15*(4), 1164–1179.
624 https://doi.org/10.1002/2013GC005122

625 Dorfman, S. M., Meng, Y., Prakapenka, V. B., & Duffy, T. S. (2013). Effects of Fe-enrichment
626 on the equation of state and stability of (Mg,Fe)SiO3 perovskite. *Earth and Planetary*
627 *Science Letters*, *361*, 249–257. https://doi.org/10.1016/j.epsl.2012.10.033
628 Du, Z., Gu, T., Dobrosavljevic, V., Weir, S. T., Falabella, S., & Lee, K. K. M. (2015). Using
629 stepped anvils to make even insulation layers in laser-heated diamond-anvil cell samples.
630 *Review of Scientific Instruments*, *86*(9), 095103. https://doi.org/10.1063/1.4929667
631 Dubrovinsky, L. S., Saxena, S. K., Lazor, P., Ahuja, R., & al, et. (1997). Experimental and
632 theoretical identification of a new high-pressure phase of silica. *Nature; London*,
633 *388*(6640), 362–365. http://dx.doi.org/10.1038/41066
634 Dziewonski, A. M., & Anderson, D. L. (1981). Preliminary reference Earth model. *Physics of the*
635 *Earth and Planetary Interiors*, *25*(4), 297–356. https://doi.org/10.1016/0031-
636 9201(81)90046-7
637 French, S. W., & Romanowicz, B. (2015). Broad plumes rooted at the base of the Earth's mantle
638 beneath major hotspots. *Nature*, *525*(7567), 95–99. https://doi.org/10.1038/nature14876
639 Frost, D. J., Liebske, C., Langenhorst, F., McCammon, C. A., & al, et. (2004). Experimental
640 evidence for the existence of iron-rich metal in the Earth's lower mantle. *Nature;*
641 *London*, *428*(6981), 409–412.
642 Frost, D. J., & McCammon, C. A. (2008). The Redox State of Earth's Mantle. *Annual Review of*
643 *Earth and Planetary Sciences*, *36*(1), 389–420.
644 https://doi.org/10.1146/annurev.earth.36.031207.124322
645 Fujino, K., Sasaki, Y., Komori, T., Ogawa, H., Miyajima, N., Sata, N., & Yagi, T. (2004).
646 Approach to the mineralogy of the lower mantle by a combined method of a laser-heated

diamond anvil cell experiment and analytical electron microscopy. *Physics of the Earth and Planetary Interiors*, *143–144*, 215–221. https://doi.org/10.1016/j.pepi.2003.11.013

Fukao, Y., Obayashi, M., & Nakakuki, T. and. (2009). Stagnant Slab: A Review. *Annual Review of Earth and Planetary Sciences*, *37*(1), 19–46. https://doi.org/10.1146/annurev.earth.36.031207.124224

Gu, T., Li, M., McCammon, C., & Lee, K. K. M. (2016). Redox-induced lower mantle density contrast and effect on mantle structure and primitive oxygen. *Nature Geoscience*, *9*(9), 723–727. https://doi.org/10.1038/ngeo2772

Hirose, K., Fei, Y., Ma, Y., & Mao, H. K. (1999). The fate of subducted basaltic crust in the Earth's lower mantle. *Nature*, *397*(6714), 53-56.

Hirose, K., Shimizu, N., Van Westrenen, W., & Fei, Y. (2004). Trace element partitioning in Earth's lower mantle and implications for geochemical consequences of partial melting at the core–mantle boundary. *Physics of the Earth and Planetary Interiors*, *146*(1-2), 249-260.

Hirschmann, M. M., Kogiso, T., Baker, M. B., & Stolper, E. M. (2003). Alkalic magmas generated by partial melting of garnet pyroxenite. *Geology*, *31*(6), 481–484. https://doi.org/10.1130/0091-7613(2003)031<0481:AMGBPM>2.0.CO;2

Hummer, D. R., & Fei, Y. (2012). Synthesis and crystal chemistry of Fe3+-bearing (Mg,Fe3+)(Si,Fe3+)O3 perovskite. *American Mineralogist*, *97*(11–12), 1915–1921. https://doi.org/10.2138/am.2012.4144

Irifune, T., & Tsuchiya, T. (2015). 2.03—Phase Transitions and Mineralogy of the Lower Mantle. In G. Schubert (Ed.), *Treatise on Geophysics (Second Edition)* (pp. 33–60). Elsevier. https://doi.org/10.1016/B978-0-444-53802-4.00030-0

Irifune, Tetsuo, Susaki, J., Yagi, T., & Sawamoto, H. (1989). Phase transformations in diopside CaMgSi2O6 at pressures Up to 25 GPa. *Geophysical Research Letters*, *16*(2), 187–190. https://doi.org/10.1029/GL016i002p00187

Jackson, M. G., Becker, T. W., & Konter, J. G. (2018). Evidence for a deep mantle source for EM and HIMU domains from integrated geochemical and geophysical constraints. *Earth and Planetary Science Letters*, *484*, 154-167.

Javoy, M. (1995). The integral enstatite chondrite model of the Earth. *Geophysical Research Letters*, *22*(16), 2219–2222. https://doi.org/10.1029/95GL02015

Jephcoat, A. P., Hemley, R. J., & Mao, H. K. (1988). X-ray diffraction of ruby (Al2O3:Cr3+) to 175 GPa. *Physica B+C*, *150*(1), 115–121. https://doi.org/10.1016/0378-4363(88)90112-X

Jephcoat, Andrew P., Mao, H. K., & Bell, P. M. (1986). Static compression of iron to 78 GPa with rare gas solids as pressure-transmitting media. *Journal of Geophysical Research: Solid Earth*, *91*(B5), 4677–4684. https://doi.org/10.1029/JB091iB05p04677

Jung, D. Y., & Schmidt, M. W. (2011). Solid solution behaviour of CaSiO3 and MgSiO3 perovskites. *Physics and Chemistry of Minerals*, *38*(4), 311–319. https://doi.org/10.1007/s00269-010-0405-0

Kaminski, E., & Javoy, M. (2015). The composition of the deep Earth. In *The Earth's Heterogeneous Mantle* (pp. 303-328). Springer, Cham.

Kaminsky, F. V., Ryabchikov, I. D., McCammon, C. A., Longo, M., Abakumov, A. M., Turner, S., & Heidari, H. (2015). Oxidation potential in the Earth's lower mantle as recorded by ferropericlase inclusions in diamond. *Earth and Planetary Science Letters*, *417*(Supplement C), 49–56. https://doi.org/10.1016/j.epsl.2015.02.029

693 Kesson, S. E., Fitz Gerald, J. D., Shelley, J. M. G., & Withers, R. L. (1995). Phase relations,
694 structure and crystal chemistry of some aluminous silicate perovskites. *Earth and*
695 *Planetary Science Letters*, *134*(1), 187–201. https://doi.org/10.1016/0012-
696 821X(95)00112-P
697 Kogiso, T., & Hirschmann, M. M. (2006). Partial melting experiments of bimineralic eclogite
698 and the role of recycled mafic oceanic crust in the genesis of ocean island basalts. *Earth*
699 *and Planetary Science Letters*, *249*(3), 188–199.
700 https://doi.org/10.1016/j.epsl.2006.07.016
701 Kurnosov, A., Marquardt, H., Frost, D. J., Ballaran, T. B., & Ziberna, L. (2017). Evidence for a
702 Fe3+-rich pyrolitic lower mantle from (Al,Fe)-bearing bridgmanite elasticity data.
703 *Nature*, *543*(7646), 543–546. https://doi.org/10.1038/nature21390
704 Lauterbach, S., McCammon, C. A., Aken, P. van, Langenhorst, F., & Seifert, F. (2000).
705 Mössbauer and ELNES spectroscopy of (Mg,Fe)(Si,Al)O3 perovskite: A highly oxidised
706 component of the lower mantle. *Contributions to Mineralogy and Petrology*, *138*(1), 17–
707 26. https://doi.org/10.1007/PL00007658
708 Lee, K. K. M., O'Neill, B., Panero, W. R., Shim, S.-H., Benedetti, L. R., & Jeanloz, R. (2004).
709 Equations of state of the high-pressure phases of a natural peridotite and implications for
710 the Earth's lower mantle. *Earth and Planetary Science Letters*, *223*(3), 381–393.
711 https://doi.org/10.1016/j.epsl.2004.04.033
712 Lundin, S., Catalli, K., Santillán, J., Shim, S.-H., Prakapenka, V. B., Kunz, M., & Meng, Y.
713 (2008). Effect of Fe on the equation of state of mantle silicate perovskite over 1Mbar.
714 *Physics of the Earth and Planetary Interiors*, *168*(1), 97–102.
715 https://doi.org/10.1016/j.pepi.2008.05.002

716 Mallik, A., Lambart, S., & Chin, E. J. (2020). Tracking the evolution of magmas from
717 heterogeneous mantle sources to eruption. *arXiv preprint arXiv:2001.00928*.
718 Mao, H. K., Chen, L. C., Hemley, R. J., Jephcoat, A. P., Wu, Y., & Bassett, W. A. (1989).
719 Stability and equation of state of CaSiO3-Perovskite to 134 GPa. *Journal of Geophysical*
720 *Research: Solid Earth*, *94*(B12), 17889–17894.
721 https://doi.org/10.1029/JB094iB12p17889
722 McCammon, C. (1997). Perovskite as a possible sink for ferric iron in the lower mantle. *Nature;*
723 *London*, *387*(6634), 694–696. http://dx.doi.org/10.1038/42685
724 McCusker, L. B., Von Dreele, R. B., Cox, D. E., Louër, D., & Scardi, P. (1999). Rietveld
725 refinement guidelines. *Journal of Applied Crystallography*, *32*(1), 36–50.
726 https://doi.org/10.1107/S0021889898009856
727 Meng, Y., Hrubiak, R., Rod, E., Boehler, R., & Shen, G. (2015). New developments in laser-
728 heated diamond anvil cell with in situ synchrotron x-ray diffraction at High Pressure
729 Collaborative Access Team. *Review of Scientific Instruments*, *86*(7), 072201.
730 https://doi.org/10.1063/1.4926895
731 Miyajima, N., Fujino, K., Funamori, N., Kondo, T., & Yagi, T. (1999). Garnet-perovskite
732 transformation under conditions of the Earth's lower mantle: An analytical transmission
733 electron microscopy study. *Physics of the Earth and Planetary Interiors*, *116*(1), 117–
734 131. https://doi.org/10.1016/S0031-9201(99)00127-2
735 Navrotsky, A., Schoenitz, M., Kojitani, H., Xu, H., Zhang, J., Weidner, D. J., & Jeanloz, R.
736 (2003). Aluminum in magnesium silicate perovskite: Formation, structure, and energetics
737 of magnesium-rich defect solid solutions. *Journal of Geophysical Research: Solid Earth*,
738 *108*(B7), 2330. https://doi.org/10.1029/2002JB002055

739 Nishiyama, N., & Yagi, T. (2003). Phase relation and mineral chemistry in pyrolite to 2200°C
740 under the lower mantle pressures and implications for dynamics of mantle plumes:
741 PHASE RELATION AND CHEMISTRY IN PYROLITE. *Journal of Geophysical*
742 *Research: Solid Earth*, *108*(B5). https://doi.org/10.1029/2002JB002216
743 Ohtani, E., & Maeda, M. (2001). Density of basaltic melt at high pressure and stability of the
744 melt at the base of the lower mantle. *Earth and Planetary Science Letters*, *193*(1), 69–75.
745 https://doi.org/10.1016/S0012-821X(01)00505-2
746 Ono, S. (2008). Experimental constraints on the temperature profile in the lower mantle. *Physics*
747 *of the Earth and Planetary Interiors*, *170*(3), 267–273.
748 https://doi.org/10.1016/j.pepi.2008.06.033
749 Ono, S., Ito, E., & Katsura, T. (2001). Mineralogy of subducted basaltic crust (MORB) from 25
750 to 37 GPa, and chemical heterogeneity of the lower mantle. *Earth and Planetary Science*
751 *Letters*, *190*(1), 57–63. https://doi.org/10.1016/S0012-821X(01)00375-2
752 Ricolleau, A., Perrillat, J.-P., Fiquet, G., Daniel, I., Matas, J., Addad, A., Menguy, N., Cardon,
753 H., Mezouar, M., & Guignot, N. (2010). Phase relations and equation of state of a natural
754 MORB: Implications for the density profile of subducted oceanic crust in the Earth's
755 lower mantle. *Journal of Geophysical Research*, *115*(B8).
756 https://doi.org/10.1029/2009JB006709
757 Ringwood, A. E., & Major, A. (1971). Synthesis of majorite and other high pressure garnets and
758 perovskites. *Earth and Planetary Science Letters*, *12*(4), 411–418.
759 https://doi.org/10.1016/0012-821X(71)90026-4

760 Shim, S.-H., Duffy, T. S., & Shen, G. (2000). The equation of state of CaSiO3 perovskite to 108
761 GPa at 300 K. *Physics of the Earth and Planetary Interiors*, *120*(4), 327–338.
762 https://doi.org/10.1016/S0031-9201(00)00154-0
763 Shim, S.-H., Grocholski, B., Ye, Y., Alp, E. E., Xu, S., Morgan, D., Meng, Y., & Prakapenka, V.
764 B. (2017). Stability of ferrous-iron-rich bridgmanite under reducing midmantle
765 conditions. *Proceedings of the National Academy of Sciences*, *114*(25), 6468–6473.
766 https://doi.org/10.1073/pnas.1614036114
767 Sinmyo, R., & Hirose, K. (2010). The Soret diffusion in laser-heated diamond-anvil cell. *Physics*
768 *of the Earth and Planetary Interiors*, *180*(3), 172–178.
769 https://doi.org/10.1016/j.pepi.2009.10.011
770 Stacey, F. D., & Davis, P. M. (2008). *Physics of the Earth*. Cambridge University Press.
771 Stixrude, L., Cohen, R., Yu, R., & Krakauer, H. (1996). Prediction of phase transition in CaSiO3
772 perovskite and implications for lower mantle structure. *American Mineralogist*, *81*(9–10).
773 https://www.degruyter.com/view/j/ammin.1996.81.issue-9-10/am-1996-9-1030/am-1996-
774 9-1030.xml
775 Stixrude, L., & Lithgow-Bertelloni, C. (2011). Thermodynamics of mantle minerals—II. Phase
776 equilibria. *Geophysical Journal International*, *184*(3), 1180–1213.
777 https://doi.org/10.1111/j.1365-246X.2010.04890.x
778 Tamai, H., & Yagi, T. (1989). High-pressure and high-temperature phase relations in CaSiO3
779 and CaMgSi2O6 and elasticity of perovskite-type CaSiO3. *Physics of the Earth and*
780 *Planetary Interiors*, *54*(3), 370–377. https://doi.org/10.1016/0031-9201(89)90254-9

781 Toby, B. H., & Dreele, R. B. V. (2013). GSAS-II: The genesis of a modern open-source all
782 purpose crystallography software package. *Journal of Applied Crystallography*, *46*(2),
783 544–549. https://doi.org/10.1107/S0021889813003531
784 Tschauner, O., Ma, C., Beckett, J. R., Prescher, C., Prakapenka, V. B., & Rossman, G. R. (2014).
785 Discovery of bridgmanite, the most abundant mineral in Earth, in a shocked meteorite.
786 *Science*, *346*(6213), 1100–1102. https://doi.org/10.1126/science.1259369
787 van Keken, P. E., Hauri, E. H., & Ballentine, C. J. (2002). Mantle Mixing: The Generation,
788 Preservation, and Destruction of Chemical Heterogeneity. *Annual Review of Earth and*
789 *Planetary Sciences*, *30*(1), 493–525.
790 https://doi.org/10.1146/annurev.earth.30.091201.141236
791 Vanpeteghem, C. B., Angel, R. J., Ross, N. L., Jacobsen, S. D., Dobson, D. P., Litasov, K. D., &
792 Ohtani, E. (2006). Al, Fe substitution in the MgSiO3 perovskite structure: A single-
793 crystal X-ray diffraction study. *Physics of the Earth and Planetary Interiors*, *155*(1-2),
794 96-103.
795 Walter, M. J., Trønnes, R. G., Armstrong, L. S., Lord, O. T., Caldwell, W. A., & Clark, S. M.
796 (2006). Subsolidus phase relations and perovskite compressibility in the system MgO–
797 AlO1.5–SiO2 with implications for Earth's lower mantle. *Earth and Planetary Science*
798 *Letters*, *248*(1), 77–89. https://doi.org/10.1016/j.epsl.2006.05.017
799 Weis, D., Garcia, M. O., Rhodes, J. M., Jellinek, M., & Scoates, J. S. (2011). Role of the deep
800 mantle in generating the compositional asymmetry of the Hawaiian mantle plume. *Nature*
801 *Geoscience*, *4*(12), 831–838. https://doi.org/10.1038/ngeo1328
802 Wilburn, D. R., & Bassett, W. A. (1978). Hydrostatic compression of iron and related
803 compounds; an overview. *American Mineralogist*, *63*(5-6), 591-596.

804 Zhuravlev, K. K., Goncharov, A. F., Tkachev, S. N., Dera, P., & Prakapenka, V. B. (2013).
805 Vibrational, elastic, and structural properties of cubic silicon carbide under pressure up to
806 75 GPa: Implication for a primary pressure scale. *Journal of Applied Physics*, *113*(11),
807 113503. https://doi.org/10.1063/1.4795348

Figures.

Figure 1. Selected quench XRD patterns with pressures given in GPa from the (**a**) reduced MIX_RED samples and (**b**) oxidized MIX_OX samples with present phases labeled as bridgmanite (bm), calcium perovskite (capv), stishovite (stv), calcium-ferrite structured phase (cf), alumina (al), neon (ne), and iron (ε-Fe). The peaks are labeled corresponding to the phase and *hkl* indices. See Figures S6 and S7 for representative Rietveld refined XRD patterns.

Figure 2. Room pressure and temperature XRD pattern for **(a)** MIX_RED and **(b)** MIX_OX with present phases labeled as bridgmanite (bm), stishovite (stv), calcium-ferrite structured phase (cf), alumina (al), rhenium (Re), and bcc iron (α-Fe). The peaks are labeled corresponding to the phase and *hkl* indices. ✦ This sample, a quenched sample held in its gasket and removed from the LHDAC, experienced blockage from the lead holder and this feature is due to the 100% line of lead which is offset from its usual d-spacing because of its different distance to the detector as compared to the sample-to-detector distance. *An anomalous peak that could not be assigned to the bridgmanite Pnma structure. The broad hump between ~2.5 – 3.5 Å and Re diffraction suggests that this pattern was collected near the edge of the gasket where the initially glass sample was unheated thus yielding an amorphous-like character.

Figure 3. Pressure versus volume of bridgmanite at room temperature, with corresponding Birch–Murnaghan equation of state curves. MIX_RED (open squares, dotted curve) and MIX_OX (filled diamonds, dashed curve) samples are shown with pressures and their uncertainties are given by error bars (see Tables S6, S7). A solid curve is shown for pure endmember $MgSiO_3$ bm (Ballaran et al., 2012).

831

832 **Figure 4.** Backscattered secondary electron (BSE) image and elemental WDS mapping of Mg, Si,
833 Fe, Al, and Ca of the quenched MIX_RED assemblage, hand-polished in cross-section. The
834 reduced assemblage is quenched from 40 GPa and 2000 K. Note that the map has several areas
835 showing elevated Fe and Al consistent with grains of metallic iron and alumina. The blacked-out
836 regions denote dust on the surface of the sample and are removed from composition analyses. The
837 dashed curve denotes the edge of the converted region within the sample. Everything to the right
838 of the dashed curve is unconverted starting material (glass powder) that is adjacent to the edge of
839 the gasket and unheated, while to the left of the dashed curve is the heated and converted sample.
840 The yellow dotted box represents chemical analysis conducted in Supporting Information (Figure
841 S8, S9, and S11).

842

843 **Figure 5.** Backscattered electron SEM image and elemental WDS mapping of Mg, Si, Fe, Al, and
844 Ca of the quenched MIX_OX assemblage, hand-polished in cross-section. The oxidized
845 assemblage is quenched from 65 GPa and 2000 K. Note that the map is very homogenous across
846 all elements.

847

848 **Figure 6.** Axial ratios of bridgmanite, **(a)** b/a and **(b)** c/a, with different compositions. Squares:
849 MIX_RED bridgmanite (this work), diamonds: MIX_OX bridgmanite (this work), solid line:
850 bridgmanite (Ballaran et al., 2012). Shaded regions denote compositions listed in Table 2: blue
851 (A): Fe^{2+}-bearing bridgmanite; purple (B): Fe^{3+}Al-bearing bridgmanite; orange (C): Fe^{3+}-bearing
852 bridgmanite; and green (D): Al-bearing bridgmanite.

853

854 **Figure 7.** Computed assemblage density as computed by BurnMan (Cottaar et al., 2014) using the
855 assemblages tabulated in Table 3 and using four different temperature profiles. (**a**) Density of 95%
856 confidence of all possible MIX_RED assemblages (white squares) based on Monte Carlo results
857 of *Models A* and *B* and MIX_OX assemblage (black diamonds) are plotted with PREM (thick gray
858 curve) as reference. All possible densities are within the thickness of each corresponding line and
859 consider four different temperature profiles: Stacy and Davis 2008; Ono 2008; Anderson et al.,
860 1982; Brown and Shankland 1981. The right axis illustrates the percent difference of each sample
861 with PREM (gray). (**b**) Computed assemblage bulk sound speed as computed by BurnMan with
862 the same constraints as (**a**). (**c**) Density of 95% confidence interval for each synthesized
863 bridgmanite from MIX_RED (white squares) and MIX_OX (black diamonds) as compared to pure
864 bridgmanite, $MgSiO_3$ (black solid line). All labels are consistent with (**a**), but Brown and
865 Shankland (1981) is applied here. Percent difference illustrates the difference between the
866 bridgmanites synthesized in this study with pure bridgmanite (gray). (**d**) Computed bulk sound
867 speed of bridgmanites from this study and pure bridgmanite. Constraints are the same as (**c**).
868
869

Tables

Table 1. Normalized chemical compositions in mol% of each oxide in the canonical pyrolite model (McDonough and Sun, 1995); pyroxenite mixture MIX1G model by Hirschmann et al., 2003; other pyroxenite assemblages P1 and P2 (Kogiso & Hirschmann, 2006); and our reduced (MIX_RED) and oxidized (MIX_OX) Al-rich pyroxenite samples based on the MIX1G pyroxenite model. To compare, see Figure S3 for a suite of natural pyroxenite compositions compared to the assemblages illustrated here. Fe^{3+} content is based on Mossbauer results (Figure S1). Note the mean molar mass of MIX_OX is ~1.8% greater than MIX_RED, due to the excess oxygens available with additional Fe^{3+} in the MIX_OX glass. Refer to Supporting Information for more information on how this data was collected and see Tables S1 and S2 for the raw data. Error bars denote two standard deviations.

* Calculated values based on Mossbauer results (Fe^{3+}/Total Fe) (Figure S1), where total FeO was measured from EPMA (Table S1 and S2).

	Pyrolite	**MIX1G Pyroxenite**	**P1**	**P2**	**MIX_RED**	**MIX_OX**
MgO	49.21	25.30	23.20	11.81	27.3(0.3)	29.2(0.4)
SiO_2	39.30	46.42	42.54	53.44	41.8(0.8)	41.1(1.0)
Al_2O_3	2.29	9.12	16.71	17.54	13.1(0.4)	13.2(0.6)
CaO	3.32	12.52	11.48	10.19	10.3(0.2)	10.7(0.2)
FeO*	5.89	6.64	6.06	7.01	7.12(0.55)	3.63(0.64)
Fe_2O_3*	-	-	-	-	0.44(0.27)	2.22(0.32)
Fe^{3+}/Total Fe	-	-	-	-	0.11(0.06)	0.55(0.08)
(Mg+Fe)/Si	1.40	0.69	0.69	0.35	0.84(0.20)	0.90(0.22)
Mean Molar Mass (g/mol)	51.87	59.18	62.74	65.51	61.1(1.10)	62.2(1.40)

887 **Table 2.** Birch-Murnaghan equations of state for bridgmanite showing errors up to 2 standard deviations
888 from this study (MIX_RED and MIX_OX); bridgmanite ($MgSiO_3$, Ballaran et al. [2012]); (A) iron-
889 bearing bridgmanite ($0.85MgSiO_3$ * $0.15FeSiO_3$) (Lundin et al., 2008); (B) Fe^{3+}, Al^{3+}-bearing bridgmanite
890 ($0.90MgSiO_3$ * $0.10FeAlO_3$) (Catalli et al. 2011); (C) Fe^{3+}-bearing bridgmanite ($0.915MgSiO_3$ *
891 $0.085Fe_2O_3$) (Catalli et al., 2010); and (D) Al^{3+}-bearing bridgmanite ($0.90MgSiO_3$ * $0.10Al_2O_3$) (Catalli et
892 al., 2011). *K_0' is fixed to a value of 4, unless otherwise noted.
893

bm composition	**V_0 (Å^3)**	**K_0 (GPa)**	**K_0'**	**Reference**
MIX_RED	163.1(0.5)	281(8)	4*	This study
MIX_OX	168.2(0.5)	284(2)	4*	This study
$MgSiO_3$	162.36(0.04)	251(2)	4*	Ballaran et al. 2012
A	163.30(0.07)	260(1)	4*	Lundin et al., 2008
B	164.81(0.04)	262(8)	3(0.3)	Catalli et al., 2011
C	165.78(0.03)	237(3)	4*	Catalli et al., 2010
D	163.83(0.05)	244(3)	4*	Catalli et al., 2011

894
895
896

Table 3. (top) Normalized bridgmanite compositions and bridgmanite room-pressure and -temperature density from each reduced (*Models A* and *B* based on the Monte Carlo results as shown in the Supporting Information: VI) and oxidized pyroxenite assemblage quenched to room conditions. The results are presented in both bridgmanite cation stoichiometry and oxide mol% (see Tables S3, S4 for raw data). MIX_RED errors are based on the Monte Carlo results; and, MIX_OX errors are based on the measurement error from the EPMA results. **(bottom)** Normalized assemblage composition for bridgmanite (bm), calcium perovskite (capv), stishovite (stv), calcium-ferrite structured phase (cf), alumina (al), iron (Fe), and total ferric iron for the entire assemblage from the quenched samples from each reduced and oxidized pyroxenite assemblage quenched to room conditions based on the Monte Carlo results as shown in the Supporting Information. Uncertainties listed represent 95% confidence intervals. *Composition of cf based on Monte Carlo modeling can be found in the Supporting Information (Figure S4c).

920

	MIX_RED, *Model A*	**MIX_RED, *Model B***	**MIX_OX**
		bm, Cations	
Mg	$0.93^{+0.03}_{-0.02}$	$0.94^{+0.03}_{-0.03}$	$0.51^{+0.02}_{-0.02}$
Si	$0.96^{+0.01}_{-0.04}$	$0.96^{+0.03}_{-0.03}$	$0.72^{+0.02}_{-0.02}$
Fe^{2+}	$0.03^{+0.05}_{-0.01}$	$0.01^{+0.02}_{-0.01}$	$0.06^{+0.02}_{-0.02}$
Fe^{3+}	$0.04^{+0.01}_{-0.01}$	$0.04^{+0.01}_{-0.01}$	$0.07^{+0.02}_{-0.02}$
Al	$0.04^{+0.08}_{-0.02}$	$0.05^{+0.08}_{-0.04}$	$0.46^{+0.02}_{-0.02}$
Ca	0	0	$0.18^{+0.02}_{-0.02}$
Sum	2.00	2.00	2.00
		bm, Oxide mol %	
MgO	$47.5^{+0.5}_{-0.5}$	$48.0^{+0.5}_{-0.5}$	$29.6^{+1.0}_{-1.0}$
SiO_2	$49.0^{+0.5}_{-0.5}$	$49.0^{+0.5}_{-0.5}$	$41.3^{+1.2}_{-1.2}$
Al_2O_3	$1.0^{+0.3}_{-0.3}$	$1.3^{+0.5}_{-0.5}$	$13.2^{+0.4}_{-0.4}$
CaO	-	-	$10.7^{+0.4}_{-0.4}$
FeO	$1.5^{+0.5}_{-1.0}$	$0.5^{+0.5}_{-0.5}$	$3.3^{+0.2}_{-0.2}$
Fe_2O_3	$1.0^{+0.3}_{-0.0}$	$1.0^{+0.5}_{-0.5}$	$2.0^{+0.2}_{-0.2}$
Sum	100	100	100
bm ρ_0 (g/cm^3)	$4.18^{+0.02}_{-0.02}$	$4.17^{+0.01}_{-0.01}$	$4.26^{+0.01}_{-0.01}$
		Phase Abundance (mol%)	
bm	50.1^{+3}_{-8}	$40.5^{+2.0}_{-2.0}$	100
capv, $CaSiO_3$	18.2^{+1}_{-1}	$18.4^{+1.0}_{-1.0}$	0
cf*, $(Mg,Fe)Al_2O_4$	12.1^{+8}_{-2}	$22.7^{+1.4}_{-1.4}$	0
al, Al_2O_3	10.4^{+4}_{-6}	0	0
stv, SiO_2	9.0^{+7}_{-2}	$18.4^{+1.5}_{-1.5}$	0
Fe	$0.17^{+0.2}_{-0.2}$	0	0
Total	100	100	100
$Fe^{3+}/\Sigma Fe$	$14^{+4}_{-3}\%$	$11^{+3}_{-3}\%$	$55^{+4}_{-4}\%$

921

922